nature metabolism

ARTICLES

https://doi.org/10.1038/s42255-020-0209-6

Check for updates

Resolution of NASH and hepatic fibrosis by the GLP-1R and GCGR dual-agonist cotadutide via modulating mitochondrial function and lipogenesis

Michelle L. Boland[1,10], Rhianna C. Laker[1,10], Karly Mather[1], Arkadiusz Nawrocki[2], Stephanie Oldham[1], Brandon B. Boland[1], Hilary Lewis[3], James Conway[4], Jacqueline Naylor[5], Silvia Guionaud[6], Michael Feigh[7], Sanne S. Veidal[7], Louise Lantier[8], Owen P. McGuinness[8], Joseph Grimsby[1], Cristina M. Rondinone[1], Lutz Jermutus[5], Martin R. Larsen[2], James L. Trevaskis[1,9] and Christopher J. Rhodes[1]✉

Non-alcoholic fatty liver disease and steatohepatitis are highly associated with obesity and type 2 diabetes mellitus. Cotadutide, a glucagon-like protein-1 receptor (GLP-1R) and glucagon receptor (GCGR) agonist, was shown to reduce blood glycaemia, body weight and hepatic steatosis in people with type 2 diabetes mellitus. Here, we demonstrate that the effects of cotadutide in reducing body weight and food intake and improving glucose control are predominantly mediated through Glp-1 signalling, whereas its action on the liver to reduce lipid content, drive glycogen flux and improve mitochondrial turnover and function are directly mediated through Gcg signalling. This was confirmed by the identification of phosphorylation sites on key lipogenic and glucose metabolism enzymes in liver of mice treated with cotadutide. Complementary metabolomic and transcriptomic analyses implicated lipogenic, fibrotic and inflammatory pathways, consistent with a unique therapeutic contribution of GCGR agonism by cotadutide in vivo. Notably, cotadutide also alleviated fibrosis to a greater extent than liraglutide or obeticholic acid, despite dose adjustment to achieve similar weight loss in two preclinical mouse models of NASH. Thus, cotadutide, via direct hepatic (GcgR) and extrahepatic (Glp-1R) effects, exerts multifactorial improvement in liver function and is a promising therapeutic option for the treatment of steatohepatitis.

Non-alcoholic fatty liver disease (NAFLD) and its progressive form, non-alcoholic steatohepatitis (NASH), are unmet medical needs affecting a substantial and increasing population[1]. Characterized by hepatic lipid accumulation, inflammation and fibrosis, NASH can lead to cirrhosis, liver failure and cancer[2,3]. As obesity and type 2 diabetes mellitus (T2DM) are major risk factors for NASH, treatments that impact body weight and glucose control have been explored[4]. Bariatric surgery is associated with increases in incretin hormones that regulate body weight and glucose metabolism[5–7]. One of these, oxyntomodulin, activates both the GLP-1 and GCG receptors (GLP-1R and GCGR) to decrease body weight via reducing food intake[8,9] and increasing energy expenditure[10]. Although GCGR agonism can relieve metabolic disease symptoms through increasing energy expenditure and reducing hepatic fat, GCG-driven hepatic glucose production is a liability by impairing glucose control. However, several studies have now demonstrated that GLP-1 can effectively counterbalance the hyperglycaemic effects of GCG[11–15].

Anti-obesity effects of dual Glp-1R/GcgR agonists were first demonstrated in diet-induced obese (DIO) mice, in which treatment with a dual agonist reduced body weight, hyperglycaemia and hepatic lipid over that of treatment with a Glp-1R agonist alone[12,16]. Our complementary work, treating overweight people with T2DM with the dual-agonist cotadutide (MEDI0382), resulted in pronounced improvement in post-prandial glucose excursions, and reductions in body weight and liver fat[11]. Others have shown that a related dual agonist can reduce liver fat and slow development of hepatic fibrosis in mouse models fed a high-fat diet (HFD) or a HFD with CCl_4 administration[17,18]. Furthermore, in methionine- and choline-deficient diet (MCD)-fed mice with partial hepatectomy, a similar dual agonist reduced inflammation, cell death and improved hepatic regeneration[19]. These data suggest that Glp-1R/GcgR agonists are potential therapeutics; however, the studies were prophylactic, rather than interventional, and not conducted in a pathophysiological relevant model of NASH[20].

Cotadutide has been engineered to balance GLP-1R and GCGR agonism (with a ~5:1 bias towards GLP-1R affinity) to optimize beneficial outcomes for metabolic disease. Here, we show cotadutide harnessed glucose- and body weight-lowering effects of Glp-1R

[1]Research and Early Development, Cardiovascular, Renal and Metabolic Diseases, BioPharmaceuticals R&D, AstraZeneca, Gaithersburg, MD, USA. [2]Department of Biochemistry and Molecular Biology, PR group, University of Southern Denmark, Odense, Denmark. [3]Research and Early Development, Oncology, AstraZeneca, Cambridge, UK. [4]Translational Sciences, AstraZeneca, Gaithersburg, MD, USA. [5]Research and Early Development, Cardiovascular, Renal and Metabolic Diseases, BioPharmaceuticals R&D, AstraZeneca, Cambridge, UK. [6]Global Pathology, AstraZeneca, Cambridge, UK. [7]Gubra, Hørsholm, Denmark. [8]Vanderbilt University Mouse Metabolic Phenotyping Center, Nashville, TN, USA. [9]Gilead Sciences, Foster City, CA, USA. [10]The authors contributed equally: Michelle L. Boland, Rhianna C. Laker. ✉e-mail: Christopher.Rhodes@astrazeneca.com

agonism while improving hepatic lipid and glucose metabolism via GcgR target engagement, to intervene and reverse NASH and hepatic fibrosis in two pathophysiologically relevant mouse models.

Results

Cotadutide's effect on body weight, food intake and glucose homeostasis is Glp-1R dependent. RNA sequencing confirmed that GLP-1R was not expressed in human liver tissue, or the non-parenchymal Kupffer or stellate cells (Supplementary Fig. 1). In contrast, GCGR was expressed in whole liver with negligible expression in Kupffer and stellate cells, implying that any impact of cotadutide on hepatic outcomes is directly mediated through GCGR signalling in hepatocytes (Supplementary Fig. 1). Metabolic and hepatic outcomes of cotadutide treatment were assessed in vivo using wild-type (WT) and Glp-1R knockout (KO) mice. Following 14 d of equimolar dosing (10 nmol per kg (body weight)) with cotadutide (dual Glp-1R/GcgR agonist), liraglutide (Glp-1R agonist) or g1437 (GcgR agonist), or co-administration of liraglutide+g1437 (5+5 nmol per kg (body weight)), body weight was markedly reduced compared with that with vehicle administration in WT mice (Fig. 1a,e). Weight-lowering effects of Glp-1R agonists in mice lacking Glp-1R were not observed when administered cotadutide or liraglutide (Fig. 1b and f). Although the Gcg-signalling component of cotadutide may hypothetically induce some weight loss independently of Glp-1, its lower potency at the GcgR produced negligible weight loss in KO animals (Fig. 1b,f). Indeed, treatment with g1437 (a more potent Gcg agonist) or liraglutide+g1437 resulted in substantial weight loss in KO mice (Fig. 1a,b). There was no effect on body composition (fat/lean mass) with any intervention (not shown). Food intake was reduced on the first 2 d of cotadutide treatment and days 2–4 of liraglutide treatment (Fig. 1c), but not in KO mice (Fig. 1d). Liver lipid content was reduced in all WT groups, by cotadutide, g1437 and liraglutide+g1437 treatments to a greater degree than by liraglutide alone (Fig. 1g). This effect was also seen in KO mice, except when treated with liraglutide alone (Fig. 1h). Fasting glucose level was lowered in WT mice treated with cotadutide and liraglutide compared with vehicle, whereas g1437 alone caused higher fasting glucose levels (Fig. 1i). Glp-1R KO mice exhibited loss of glucose control and did not respond to any treatments (Fig. 1j,l,n). During intraperitoneal glucose tolerance test (ipGTT), liraglutide reduced blood glucose compared with that after vehicle treatment in WT mice, and a similar trend was observed with cotadutide (Fig. 1k,m). Treatment with g1437 or liraglutide+g1437 resulted in much higher blood glucose during ipGTT (Fig. 1k,m). Plasma insulin was lower in all WT animals under all treatment conditions, as compared with vehicle treatment, but was lower in KO animals only following g1437 or liraglutide+g1437 (Fig. 1q,r). Endogenous plasma Gcg was suppressed in groups treated with a therapeutic GcgR agonist regardless of genotype (Fig. 1o,p). Plasma leptin, a marker of fat mass, was lower in all WT animals following treatment. In the absence of Glp-1R, plasma leptin remained lower in mice treated with a GcgR agonist, whereas liraglutide had no effect (Fig. 1s,t). These data demonstrate that metabolic benefits of cotadutide are mediated through Glp-1 action, whereas improvements in hepatic lipid content are mediated through GcgR activation.

Cotadutide reduces hepatic lipid content and alters carbohydrate flux in DIO mice. Temporal effects of cotadutide, liraglutide, g1437 and liraglutide+g1437 on metabolic and hepatic parameters were assessed after daily dosing of DIO male mice for 7 d, and there was weight loss in all groups relative to that in the vehicle group (Fig. 2a and Supplementary Fig. 2). All groups that received a GcgR agonist displayed lower hepatic lipid content than those that received vehicle, unlike liraglutide (Fig. 2b and Supplementary Fig. 2). After dosing, the serum cotadutide concentration was highest at 2 h and 6 h, but undetectable at 16 h (Fig. 2c,d and Supplementary Fig. 2e). On the basis of pharmacokinetics, levels of liraglutide were estimated to be lower (~50%) but with longer bioavailability, whereas estimated g1437 concentrations were ~30% that of cotadutide with similar clearance (Fig. 2c,d). Blood glucose was not different between groups across the time course (Fig. 2e), but, in a smaller study of vehicle versus cotadutide treatment, cotadutide significantly ($P = 0.0002$) lowered blood glucose at 2 h and 6 h (Supplementary Fig. 2e).

Plasma insulin in the vehicle-treated group increased at 6 h post dose (Fig. 2f and Supplementary Fig. 2c) corresponding to increased food intake. Plasma Gcg was elevated in vehicle-treated animals (Fig. 2g and Supplementary Fig. 2d) and reduced in liraglutide-treated animals (Fig. 2g). In all groups treated with a therapeutic Gcg agonist, endogenous Gcg secretion was suppressed (Fig. 2g and Supplementary Fig. 2d). Liver glycogen was elevated prior to the final dose of cotadutide and rapidly depleted by 6 h post cotadutide treatment, but rebounded to normal at 16 h (Fig. 2h and Supplementary Fig. 2f). g1437 and liraglutide+g1437 treatment produced similar rapid depletion, although less restoration of liver glycogen, whereas liraglutide alone did not differ from vehicle (Fig. 2h).

Dynamic changes in liver glycogen and lipid content were evaluated using hyperglycaemic clamps to induce a fed-like state and stimulate hepatic glucose uptake, glycogen synthesis and de novo lipogenesis (Fig. 3a). Hepatic glycogen depletion following cotadutide administration was observed, as indicated by lower core glycogen levels (that is, glycogen that had not incorporated radio-labelled glucose) (Fig. 3b,i). This is consistent with increased basal glucose production that was preferentially generated through gluconeogenesis, and not glycogenolysis (Fig. 3c–e). Liraglutide had no impact on core glycogen, but g1437 resulted in severely depleted hepatic glycogen following fasting (Fig. 3b), consistent with GcgR activation resulting in lower glycogenolysis (Fig. 3e). Glycogen synthesis, stimulated by hyperglycaemia, was intact in cotadutide-treated mice, liraglutide augmented direct glycogen synthesis and g1437 strongly decreased both direct and indirect synthesis (Fig. 3f–h). Importantly, hepatic glucose production in cotadutide-treated mice was suppressed during hyperglycaemia (Fig. 3j), whereas g1437 limited suppression of endogenous glucose production (Fig. 3j–l).

Cotadutide reduced de novo lipogenesis during the clamp, as shown by reduced palmitate and glyceride synthesis (that is, lipids that have incorporated radio-labelled ^2H_2O), contributing to lower levels of total hepatic palmitate and glyceride (Fig. 3m–p). Liraglutide had no effect, but g1437 dramatically reduced lipid synthesis, resulting in a similar overall effect to that of cotadutide (Fig. 3m–p). These novel tracer experiments demonstrate that the balance of Gcg tone and Glp-1 activity by cotadutide allows for hepatic metabolic switching in response to glycaemic status.

Metabolomic analysis revealed that, at 6 h post treatment, both 3-phosphoglycerate and phosphoenolpyruvate, metabolites of glycolysis and gluconeogenesis, were elevated in livers of cotadutide-treated mice (Supplementary Table 1). All metabolites of the pentose phosphate pathway (PPP) detected were increased with cotadutide treatment, while tricarboxylic acid (TCA) cycle intermediates were unchanged or reduced (Supplementary Table 1). Multiple glucogenic and ketogenic amino acids were reduced in cotadutide-treated liver compared with vehicle-treated liver at 6 h, along with increased AMP and ADP levels (Supplementary Table 1). These data, in the context of altered corresponding blood glucose and liver glycogen, suggest that gluconeogenic precursors may be shunted through the PPP in cotadutide-treated mice.

To understand sub-chronic effects of cotadutide, we compared the hepatic and metabolic outcomes with liraglutide, g1437 or the combination liraglutide+g1437 in C57BL6J diet-induced NASH model. Cotadutide reduced body weight similarly to liraglutide+g1437, but more than either liraglutide or g1437 alone (Extended Data Fig. 1a).

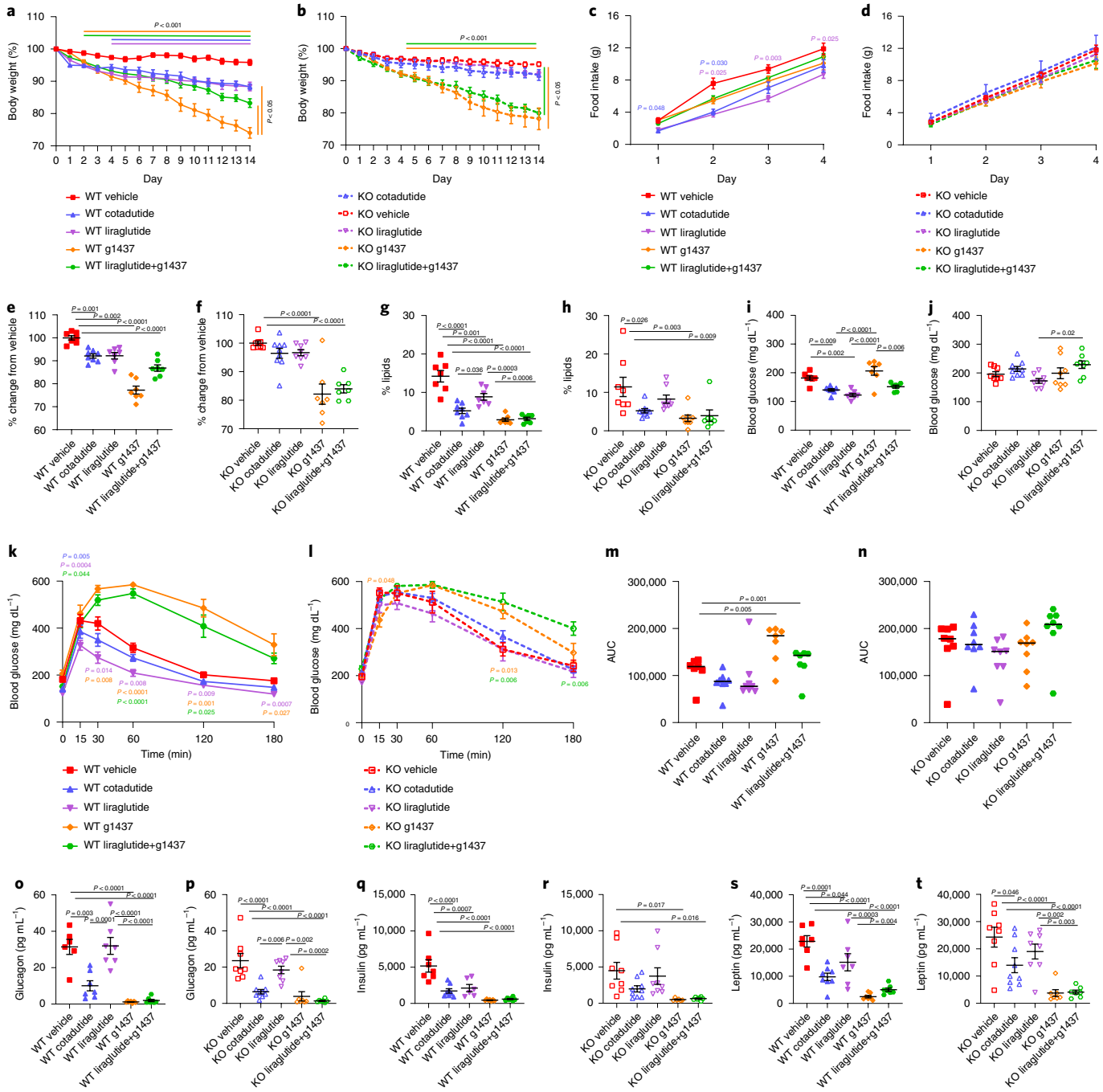

Fig. 1 | Metabolic and hepatic parameters following 2-week treatment of DIO Glp-1R WT or KO mice with cotadutide, liraglutide, g1437 or liraglutide+g1437. Mice received equimolar dosing (10 nmol per kg (body weight) subcutaneously (SC), once daily (QD) for 14 d. Blood and tissues were collected 20 h after administration of the final dose. Animals were given ad libitum access to food for the entirety of the study except for the day of GTT on which they were fasted for 6 h prior to injection of glucose (1.25 mg per kg (body weight)). **a**,**b**, Reduction in body weight throughout the 14-d dosing period is shown as percentage change in WT (**a**) and KO (**b**) mice. **c**,**d**, Cumulative food intake during the first 4 d of dosing in WT (**c**) and KO (**d**) mice. **e**,**f**, Percentage change in body weight from vehicle in WT (**e**) and KO (**f**) mice. **g**,**h**, Terminal (last day of treatment) liver lipid percentage in WT (**g**) and KO (**h**) mice. **i**–**n**, Fasting blood glucose levels, blood glucose profile during ipGTT and area under the glucose curve in WT (**i**, **k** and **m**, respectively) and KO mice (**j**, **l** and **n**, respectively). **o**–**t**, Plasma glucagon, insulin and leptin in WT (**o**, **q** and **s**, respectively) and KO (**p**, **r** and **t**, respectively) mice. WT vehicle ($n = 7$); WT cotadutide ($n = 8$); WT liraglutide ($n = 7$); WT g1437 ($n = 7$); WT liraglutide+g1437 ($n = 7$); KO vehicle ($n = 8$); KO cotadutide ($n = 9$); KO liraglutide ($n = 8$); KO g1437 ($n = 8$); KO liraglutide+g1437 ($n = 7$) mice per group. Data are shown as the mean ± s.e.m. Statistical tests were two-way analysis of variance (ANOVA) (**a**–**d**,**k**,**l**) and one-way ANOVA with post hoc Tukey's multiple comparison test (**e**–**j**,**m**–**t**). In **a** and **b**, lines above the graph indicated differences compared with vehicle at each time point, and lines to the right indicated differences between groups at day 14. In **c**, **k** and **l**, *P* values in colour represent the treatment group indicated versus vehicle.

A pyruvate tolerance test revealed lower glucose excursion in cotadutide-treated animals (Extended Data Fig. 1b,c). Fasted insulin was also lower in cotadutide-treated animals than those treated with vehicle, liraglutide or liraglutide+g1437 (Extended Data Fig. 1d). Fasted glucose was appreciably higher in g1437-treated animals and in combination with liraglutide (Extended Data Fig. 1e). Plasma

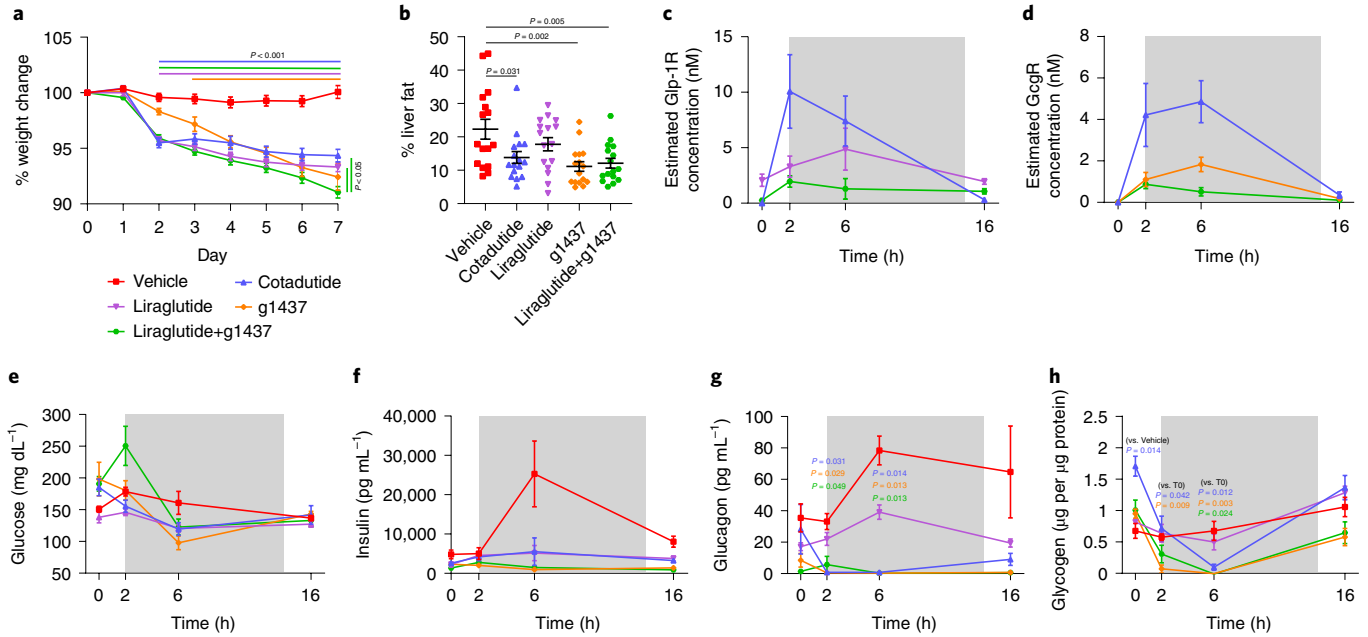

Fig. 2 | Temporal changes in metabolic and hepatic parameters following 1-week treatment of DIO C57Bl6/J mice with cotadutide, liraglutide, g1437 or liraglutide+g1437. Mice received equimolar dosing (10 nmol per kg (body weight) subcutaneously (SC), once daily (QD) for 7 d. Blood and tissues were collected at indicated time points after administration of the final dose. Animals were given ad libitum access to food for the entirety of the study. **a**–**h**, Reduction in body weight throughout the 7-d dosing period shown as percentage change from baseline (**a**), terminal liver lipid percentage (**b**), serum Glp-1R bioactivity profiles for cotadutide and liraglutide treatments (**c**), serum GcgR bioactivity profiles for cotadutide and g1437 treatments (**d**), blood glucose levels (**e**), plasma insulin levels (**f**), plasma glucagon (**g**) and liver glycogen content (**h**). For **c**–**h**, grey area indicates lights out. For each time point, $n = 4$ mice per group. Data are shown as the mean ± s.e.m. Statistical tests were two-way ANOVA (**a**,**c**–**h**) or one-way ANOVA, with post hoc Tukey's multiple comparison test (**b**). In **a**, lines above the graph indicate differences compared with vehicle at each time point, and lines to the right indicated differences between groups at day 7. In **g**, *P* values indicate differences compared with vehicle at each time point for the indicated group.

alanine aminotransferase (ALT) was reduced in animals treated with cotadutide, g1437 or liraglutide+g1437, but was unchanged by liraglutide treatment alone (Extended Data Fig. 1f). Hepatic glycogen was reduced in NASH vehicle and elevated only with cotadutide treatment. Triglycerides were elevated with NASH and reduced in mice treated with cotadutide, g1437 or liraglutide+g1437 (Extended Data Fig. 1g,h). Hepatic cholesterol increased with NASH and reduced in the g1437 and liraglutide+g1437 groups (Extended Data Fig. 1i). Altogether, these data suggest that cotadutide dual-agonism promotes optimal hepatic and metabolic benefits of Glp-1R and GcgR action.

Cotadutide induces hepatic phosphoproteomic changes and reveals new targets of hepatic GcgR signalling. The hepatic phosphoproteome in response to cotadutide was investigated in the mouse cohort presented in Supplementary Fig. 2. Phosphorylation of 5′ AMP-activated protein kinase-α (Ampkα) and Ampkβ subunits were increased 2 h and 6 h after administration of cotadutide relative to that following vehicle treatment (Fig. 4a), at Thr490, Ser496 and Ser508 of Ampkα1, Thr172 and Ser481 of Ampkα2 and Ser24 and Ser25 of Ampkβ1 (Fig. 4a and Supplementary Table 2). Cotadutide induced changes in phosphorylation for numerous proteins involved in carbohydrate (Fig. 4b) and lipid (Fig. 4c) metabolism, including cAMP-response element binding protein (Chrebp), acetyl CoA carboxylase 2 (Acc2) and ATP-citrate lyase (Acly) (Fig. 4c and Supplementary Table 2).

We determined which phosphorylation changes detected in vivo were due to Gcg-driven signalling in hepatocytes. Numerous new phospho-sites were detected for molecules associated with cellular metabolism (Fig. 4d). Six were reported Pka substrates, including Ampk catalytic subunit α1 (phosphorylated at Ser496 (p-S496)), Ampk non-catalytic subunit β1 (p-Ser24), glycogen synthase kinase-3 alpha (Gsk3a p-S21), phosphorylase b kinase regulatory subunit beta (Phkb p-S19), Chrebp (p-S196) and hormone sensitive lipase (Hsl p-S557) (Fig. 4d and Extended Data Fig. 2). We mined data compiled on PhosphoSitePlus to further investigate the remaining sites. Twenty of the phosphorylated sites contain Pka consensus motifs, and an additional 11 do not (Fig. 4d). Aside from six previously identified Pka targets, all but four of the detected phospho-sites were previously reported. Phosphorylase b kinase regulatory subunit alpha, liver isoform (Phka2 p-S640), glycogen phosphorylase, liver form (Pygl p-T214 and p-T520) and Chrebp (p-S195) do not contain PKA consensus motifs, indicating they may be targets of other downstream kinases (Fig. 4d and Extended Data Fig. 2). Phosphoproteomic analysis does not detect all phosphoproteins, and some known phosphorylation sites downstream of glucagon, such as pCreb, did not survive the stringent 1% false-discovery rate cut-off. However, key phosphoproteins, including pPka and pCrtc3, were detected, supporting reliability of the phosphoproteomic dataset.

Multiple enzymes involved in the lipid-synthesis pathway were phosphorylated following g1437 treatment, including Acly (p-S455), Acc2 (p-S81) and diacylglycerol *O*-acyltransferase (Dgat1, p-T15/p-S20, p-S17/p-S20 and p-S20) (Fig. 4d). Phosphorylation of these enzymes is predicted to inhibit their activity, complementary to reduced de novo lipid synthesis in primary mouse hepatocytes treated with g1437 or cotadutide, but not liraglutide (Fig. 4e). Incubation with H89, a Pka inhibitor, or U73122, a phospholipase C inhibitor, failed to alleviate cotadutide-mediated suppression of de novo lipogenesis, indicating this may not necessarily be mediated by Pka or phospholipase C (Supplementary Fig. 3). Pharmacological inhibition of other kinases (rapamycin to inhibit mTOR, SB 203580 to inhibit p38Mapk, compound C to inhibit Ampk, LY-294 to inhibit Pi3k and PD98 to inhibit Mapkk) all failed to block the suppression

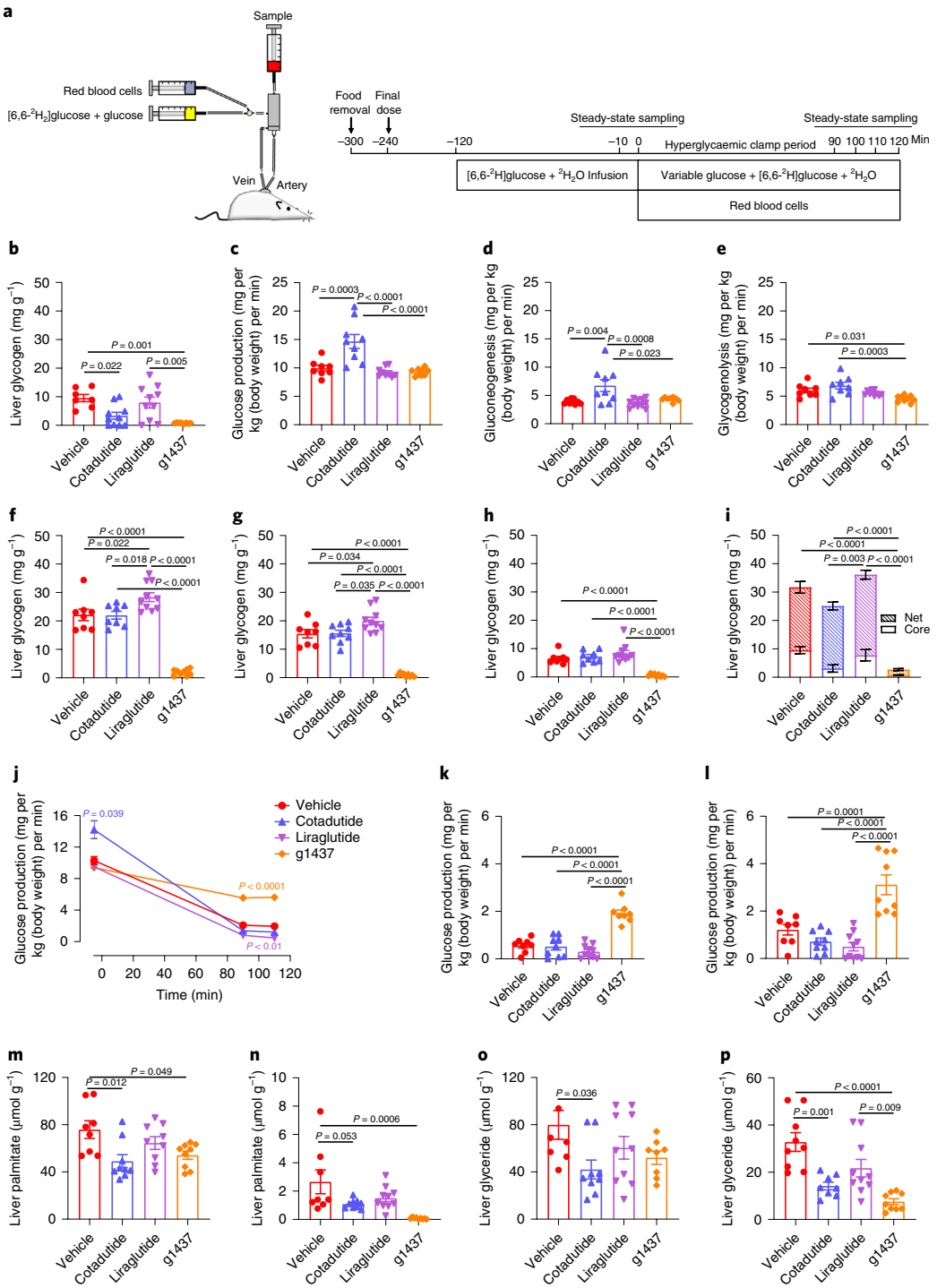

Fig. 3 | Hepatic glycogen flux following 1-week treatment of DIO C57Bl6/J mice with cotadutide, liraglutide or g1437. Mice received equimolar dosing (10 nmol per kg (body weight) subcutaneously (SC), once daily (QD) for 7 d. **a**, Experimental design showing continuous infusion of [6,6-$^2H_2$]glucose and ^2H_2O was initiated 2 h following the final dose in fasted animals for 120 min to achieve steady state, and then for an additional 120 min with hyperglycaemia. **b**, Levels of core hepatic glycogen. This is the liver glycogen content that does not contain radio-labelled glucose, indicating that it was synthesized prior to initiation of the infusion. **c**–**e**, Glucose production (**c**), gluconeogenesis (**d**) and glycogenolysis (**e**) during the fasted, basal state. **f**–**h**, Net glycogen synthesis (**f**) and direct (**g**) and indirect (**h**) glycogen synthesis, which are indicative of incorporation of glucose directly from the circulation or indirectly from diversion of gluconeogenic carbon to glycogen, respectively. **i**, Total liver glycogen at the conclusion of the experiment, showing the net and core glycogen contributions. **j**–**l**, Endogenous glucose production (**j**), gluconeogenesis (**k**) and glycogenolysis (**l**) during the hyperglycaemic clamp. **m**,**n**, Total (**m**) and newly synthesized (**n**) hepatic palmitate during ^2H_2O infusion. **o**,**p**, Total (**o**) and newly synthesized (**p**) hepatic glyceride during ^2H_2O infusion. Vehicle ($n = 8$); cotadutide ($n = 9$); liraglutide ($n = 10$); g1437 ($n = 9$) mice per group. Data are shown as the mean ± s.e.m. Statistical tests were one-way (all panels but **j**) and two-way (**j**) ANOVA with post hoc Tukey's multiple comparison test. In **j**, coloured *P* values represent the difference of the indicated group compared with the vehicle group.

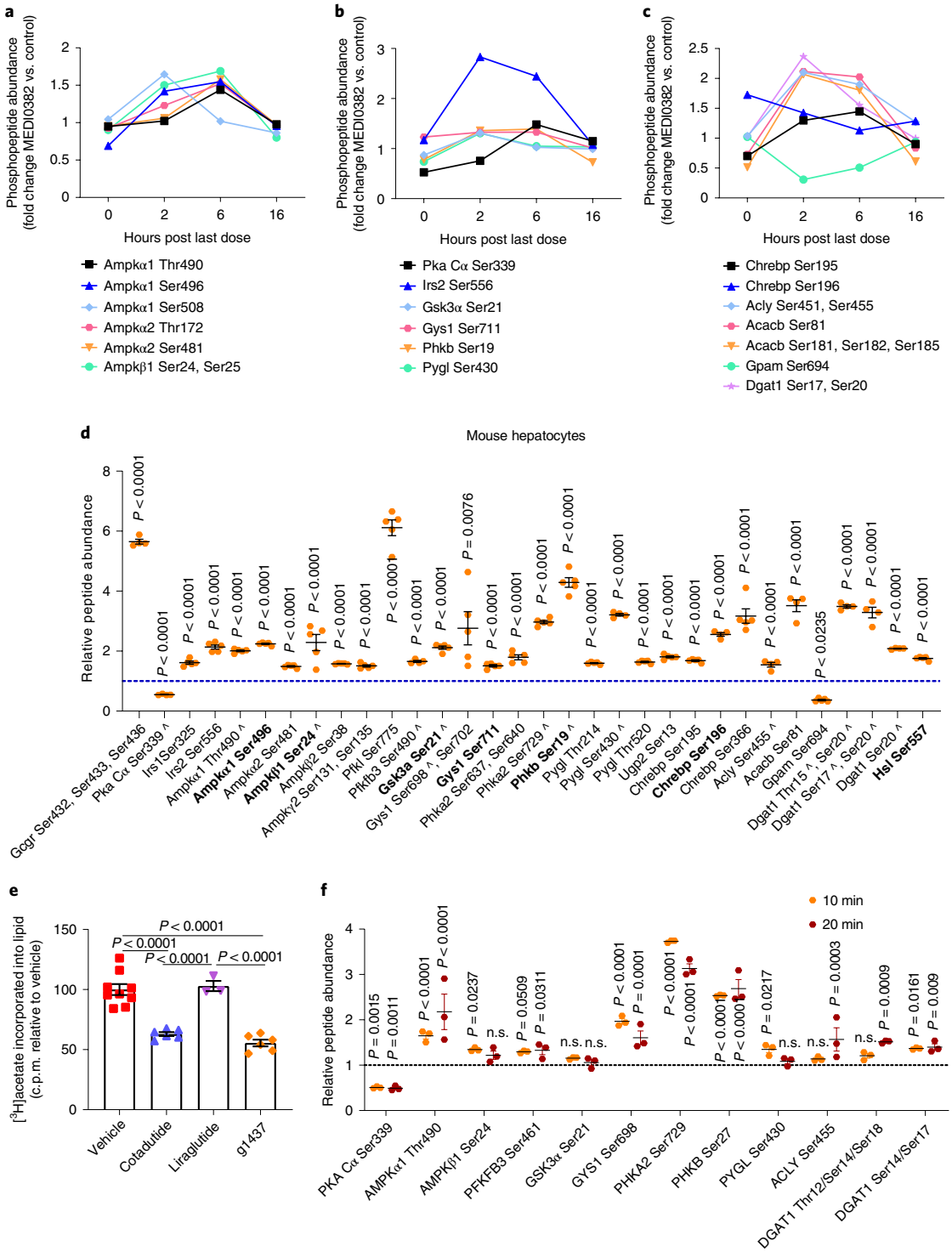

Fig. 4 | Cotadutide-induced changes in the hepatic phosphoproteome of carbohydrate-metabolism- and lipid-metabolism-related molecules. **a**–**c**, Hepatic phospho-sites of Ampkα and Ampkβ (**a**), proteins involved in glucose metabolism (**b**) and proteins involved in lipid metabolism (**c**) detected in DIO mice following repeated dosing of cotadutide (10 nmol per kg (body weight), SC, QD for 7 d) compared with vehicle treatment. Livers were collected at the indicated time points after administration of the final dose. For each time point, $n = 3$ mice per group. Adjusted P values from built-in ANOVA are shown in Supplementary Table 2. **d**, Differential abundance of phosphorylated peptides detected in primary murine hepatocytes following a 10-min treatment with 100 nM g1437, a GcgR agonist. Abundance in g1437-treated cells relative to unstimulated control cells ($n = 5$ per group). The experiment was replicated on two separate occasions, yielding similar results. Bold text indicates known Pka-targeted sites; ^ indicates homologous sites identified in human hepatocytes. **e**, De novo lipogenesis in primary murine hepatocytes treated ex vivo with 100 nM cotadutide ($n = 6$), 100 nM g1437 ($n = 6$) or 100 nM liraglutide ($n = 3$) shown as [^{3}H]acetate lipid incorporation relative to that in vehicle-treated controls ($n = 9$). Sample size indicates biologically independent experiments and data are shown as the mean ± s.e.m. **f**, Differential abundance of phosphopeptides detected in primary human hepatocytes following a 10- or 20-min treatment with 100 nM g1437. Abundance in g1437-treated cells relative to unstimulated control cells ($n = 3$ biologically independent samples per group). In **d**–**f**, data are shown as mean ± s.e.m. For statistical analysis in **d** and **f**, comparisons were versus unstimulated controls, using two-sided Student's t-test; and in **e**, comparisons were versus vehicle controls, using one-way ANOVA with post hoc Tukey's multiple comparison test.

of de novo lipogenesis induced by cotadutide (Supplementary Fig. 3). Twelve homologous phospho-sites were detected following g1437 treatment of primary human hepatocytes (Fig. 4f), supporting the relevance of our findings in mice to human biology.

Cotadutide induces mitochondrial turnover and enhances mitochondrial function. Hepatic mitochondrial dysfunction and oxidative stress have been implicated in NASH pathogenesis[21], and whether cotadutide could alter mitochondrial dynamics and function was examined in primary mouse hepatocytes. Increased number of green-labelled mitochondria within red-labelled lysosomes (here termed mitophagosomes) were observed in both cotadutide- and g1437-treated cells compared with vehicle-treated cells (Fig. 5a,b), without altering mitochondrial number (Supplementary Fig. 4).

The transcriptional induction of the mitochondrial biogenesis regulator *Ppargc1a* (also known as Pgc-1α) downstream of Gcg and Pka signalling is known. Cotadutide and g1437 equally increased *Ppargc1a* messenger RNA in a concentration-dependent manner, via Pka signalling (Fig. 5c). Other genes known to be induced downstream of GcgR and Pka activation, *G6pc* and *Pck1*, were also induced by cotadutide and g1437 (Extended Data Fig. 3). In primary human hepatocytes from both healthy donors and those with NASH, cotadutide and g1437 substantially increased *PPARGC1A* transcript levels (Fig. 5d). Liraglutide had no effect (Fig. 5c,d).

We examined whether cotadutide-mediated improvement in mitochondrial maintenance benefited mitochondrial function. Hepatocytes from *ob/ob* NASH mice displayed notably reduced basal and maximal oxygen-consumption rate (OCR) compared with that in lean controls (Fig. 5e–g), as previously observed[22,23]. Ex vivo treatment with cotadutide or g1437, but not liraglutide, restored basal and maximal respiratory rates in NASH hepatocytes to similar levels as those in normal controls (Fig. 5e–g). Treatment of healthy mouse primary hepatocytes with cotadutide or g1437 also increased basal and maximal respiration rates (Extended Data Fig. 4a–c). Ex vivo treatment with cotadutide or g1437 had no effect on fuel preference (Extended Data Fig. 4d). This improved mitochondrial function was mediated by GcgR downstream signalling. When Pka, Plc, p38Mapk and Ampk were inhibited, cotadutide was unable to increase OCR in the hepatocytes (Fig. 5h,i, Extended Data Fig. 4e,f and Supplementary Fig. 5a–d). Inhibition of mTOR or non-GcgR-mediated pathways, including Mapkk and Pi3k, resulted in the normal cotadutide-induced increase in OCR (Extended Data Fig. 4g–i and Supplementary Fig. 5e–g). These data demonstrate that cotadutide increases mitochondrial turnover and improves mitochondrial oxidative capacity directly via GcgR signalling.

Superior efficacy of cotadutide in alleviating NASH in vivo. Cotadutide treatment was compared with liraglutide and the synthetic bile acid and farnesoid X-receptor (FXR) agonist obeticholic acid (OCA) in a physiologically relevant mouse model of NASH. Cotadutide and liraglutide doses were deliberately adjusted to achieve similar weight loss, ~8% from baseline, whereas OCA had a lesser effect with only ~3% reduction (Fig. 6a). Both cotadutide and liraglutide reduced food intake within the first 4 d, with OCA having no effect (Fig. 6b). Glucose tolerance was markedly improved by cotadutide, moreso than by liraglutide or OCA (Fig. 6c,d). Plasma insulin increased at 15 min in the cotadutide versus liraglutide group during the ipGTT, and OCA had no effect (Fig. 6e).

Terminal non-fasted blood glucose and plasma insulin, triglycerides, cholesterol and aspartate aminotransferase (AST) were increased with NASH (Supplementary Table 3). OCA, compared with vehicle, reduced plasma cholesterol, whereas cotadutide and liraglutide reduced glucose and cholesterol (Supplementary Table 3). NASH increased liver mass (Fig. 6f) and plasma ALT (Fig. 6g). Liraglutide, compared with vehicle, reduced liver mass and ALT levels, with OCA only reducing liver mass (Fig. 6f,g). Cotadutide reduced ALT levels (Fig. 6g), and the increase in hepatic glycogen (Fig. 6h) probably accounted for unchanged liver mass in the face of reduced liver lipids (Fig. 6i–l). Metabolomics analysis demonstrated increased hepatic glycogen synthesis and degradation intermediates following cotadutide treatment (Supplementary Fig. 6).

Serum and liver lipidomics revealed that NASH reduced serum, but increased hepatic, levels of triglycerides (TAG), diglycerides (DAG), cholesterol esters (CE) and free fatty acids (FFA), as compared with control levels (Fig. 6i–l). All therapeutic treatments resulted in reduction of hepatic TAG, DAG and FFA, and serum and hepatic CE, with cotadutide having a more profound effect than liraglutide and a similar effect to OCA (Fig. 6i–l).

Hepatic fibrosis is a key characteristic of NASH pathogenesis. NASH mice exhibited stable fibrosis, during the treatment period, with 1/12 animals (8.3%) showing worsened fibrosis (Fig. 6r and Supplementary Figs. 7 and 8). All treatments induced reductions in fibrosis to some degree: liraglutide and OCA groups had 1/12 animals (8.3%) and cotadutide had 3/12 (25%) with reduced fibrosis (Fig. 6r and Supplementary Figs. 7 and 8). Cotadutide was the only treatment with which no animals had worsened fibrosis (Fig. 6r and Supplementary Figs. 7 and 8). Unlike humans, 'hepatocyte ballooning', which is indicative of hepatocyte degeneration and death, is extremely rare in rodent NASH models and thus the NAFLD activity score (NAS) is predominately driven by steatosis and inflammation. Cotadutide treatment led to many more animals with lower steatosis and inflammation scores and overall NAS (Fig. 6n–q and Supplementary Figs. 7 and 8). Transcriptome signatures specific to metabolism were enriched in chow controls compared with NASH mice (Supplementary Fig. 9 and Supplementary Tables 4 and 5). Cotadutide treatment was quite different than NASH vehicle for a predicted peroxisome pathway (Supplementary Fig. 9a and Supplementary Table 5). Biocarta signatures related to inflammation and fibrosis showed appreciable differences between control and NASH mice in the interleukin-17 (Il-17) pathway, fibrinolysis pathway, Il-12 pathway and platelet-derived growth factor (Pdgf) pathway (Supplementary Fig. 9b and Supplementary Table 5). Liraglutide and OCA treatment had no particular impact on any pathway, whereas cotadutide trended to impact the Il-17 and the fibrinolysis pathways relative to the effects of vehicle (Supplementary Fig. 9b and Supplementary Table 5). Signatures for transforming growth factor β (Tgfβ) signalling, interferon-α response, inflammatory response and apoptosis were all relatively different between controls and NASH (Supplementary Fig. 9c and Supplementary Table 5). Cotadutide and OCA groups showed more separation on the PCA plot from NASH vehicle, whereas liraglutide-treated animals did not separate (Supplementary Fig. 9d).

Cotadutide is more effective at reducing hepatic steatosis. The effect of cotadutide was examined on metabolic and liver end points in a more severe *ob/ob* mouse NASH model, compared with vehicle controls (AMLN, vehicle), liraglutide and a control group switched back to low-fat diet (LFD) and administered vehicle. Again, cotadutide (30 nmol per kg (body weight)) and liraglutide (40 nmol per kg (body weight)) were dose-adjusted to achieve similar weight loss of ~7–8% from baseline (Fig. 7a). Switching from AMLN to LFD transiently prevented weight gain between days 15–20 (Fig. 7a). There were no differences in body composition between groups (Fig. 7b). Cotadutide- and liraglutide-treated animals had similar improved glucose control to that in animals treated with AMLN or vehicle (Fig. 7c,d). NASH induction increased fed plasma insulin, TAGs and cholesterol, with cotadutide and liraglutide reducing plasma cholesterol (Supplementary Table 6). Liver mass was increased with NASH and similarly reduced by cotadutide and liraglutide (Fig. 7e).

Macro- and microsteatotic lipid droplets were increased in NASH but reduced by cotadutide (Fig. 7f), complementary to a

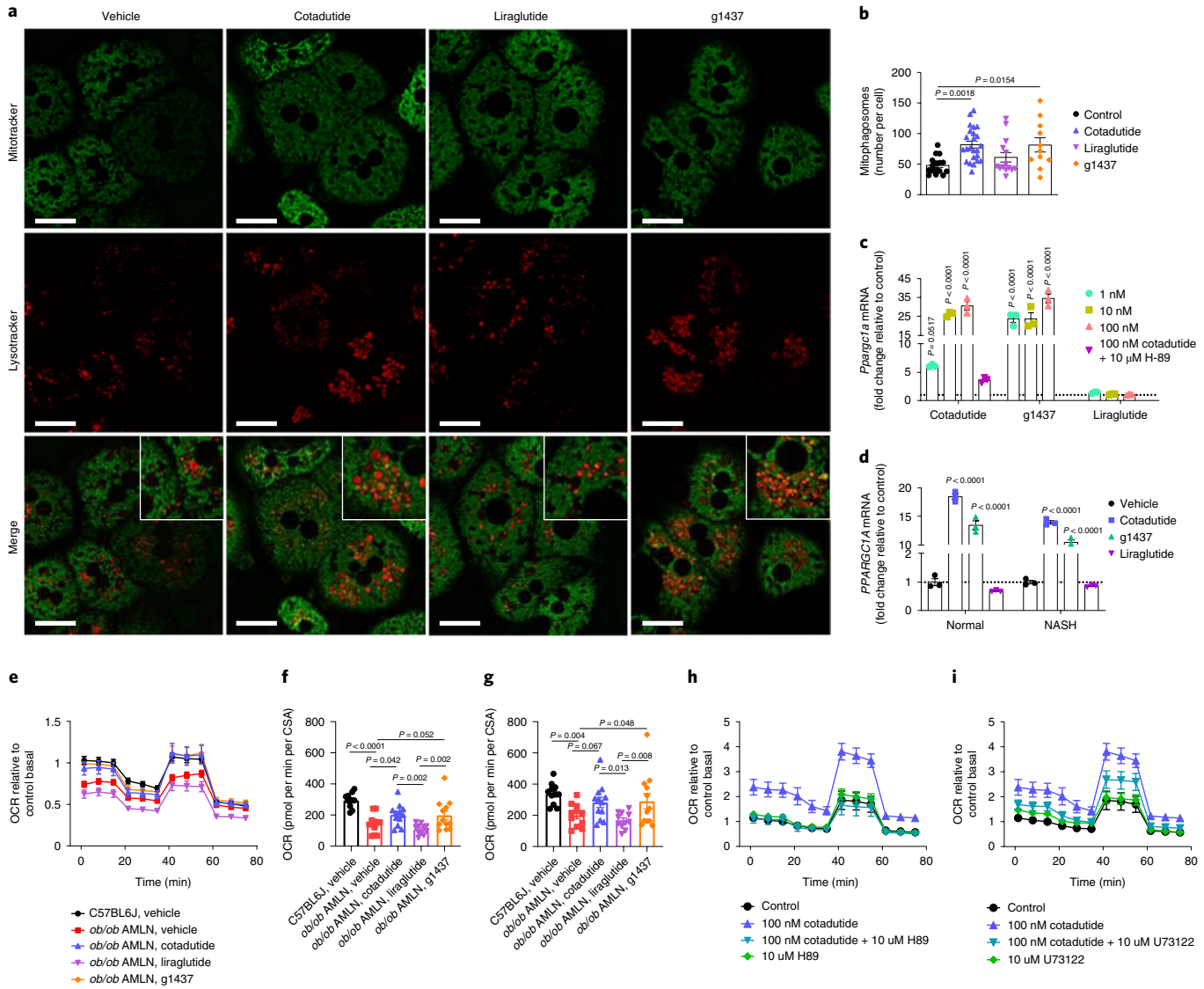

Fig. 5 | Cotadutide induces mitochondrial turnover and improves mitochondrial respiration. a, Representative live cell confocal microscopy images showing mouse primary hepatocytes treated ex vivo with 100 nM cotadutide, g1437 or liraglutide for 2 h and stained with Mitotracker Green and Lysotracker Deep Red. Scale bars, 25 μm. **b**, Quantification of Lysotracker Deep Red puncta that contain Mitotracker Green as a measure of mitophagosomes; control ($n = 15$); cotadutide ($n = 24$); liraglutide ($n = 14$); g1537 ($n = 11$) cells per treatment. **c**, *Ppargc1a* mRNA levels in primary mouse hepatocytes treated with increasing concentrations (1, 10 and 100 nM) of cotadutide, g1437 or liraglutide for 4 h. Cells were also treated with 100 nM cotadutide plus 10 μM H89; $n = 3$ biologically independent samples per group. **d**, *PPARGC1a* mRNA in primary human hepatocytes from healthy donors or those with NASH, treated with 100 nM cotadutide, g1437 or liraglutide for 4 h; $n = 3$ biologically independent samples per group. **e**, OCR during mitochondrial stress test of primary hepatocytes from obese (*ob/ob*) mice with NASH treated ex vivo for 4 h with 100 nM cotadutide ($n = 12$) or 100 nM liraglutide ($n = 11$) or g1437 ($n = 11$), compared with untreated NASH hepatocytes ($n = 11$). Respiration of untreated primary hepatocytes from lean C57BL6/J controls ($n = 3$) is also shown. (Sample size indicates number of replicates from a single biological sample. The experiment was repeated three times with similar results.) **f**,**g**, Basal (**f**) and maximal (**g**) respiration from hepatocytes in **e**. **h**,**i**, Oxygen consumption of healthy mouse primary hepatocytes treated with cotadutide with or without PKA inhibitor, H89 (**h**; 10 μM) or PLC inhibitor, U73122 (**i**; 10 μM). ($n = 6$ replicates for a single biological sample. The experiment was repeated three times with similar results.) All data are shown as the mean ± s.e.m. For statistical analysis in **b**–**d**, comparisons were versus vehicle controls, using one-way ANOVA with Dunnett's multiple comparisons post hoc test; and in **f** and **g**, a two-sided Student's *t*-test was used for C57BL6/J, vehicle versus *ob/ob* AMLN, vehicle to determine effect of diet, and a one-way ANOVA with post hoc Tukey's multiple comparison test used for treatment effect with C57BL6/J, with the vehicle group excluded.

substantial reduction in hepatic lipid content compared with that following liraglutide and a diet switch (Fig. 7g). TAGs and CEs, but not FFAs, DAGs or ceramides, were increased in AMLN vehicle mice compared with LFD mice (Fig. 7h–l). FFAs were increased by diet switching (Fig. 7h). All treatments, compared with vehicle treatment, reduced hepatic TAGs, but only cotadutide additionally reduced DAGs and ceramides (Fig. 7i,j,l). Long-chain acyl carnitine species were increased in LFD controls but decreased in cotadutide-treated mice compared with those treated with vehicle (Fig. 7m and Supplementary Table 7).

Metabolomics indicated propionylcarnitine, a product of amino acid catabolism, was increased in cotadutide-treated livers compared with those treated with vehicle (Fig. 7m). Ketone body 3-hydroxybutyrate was increased in LFD and with all treatments

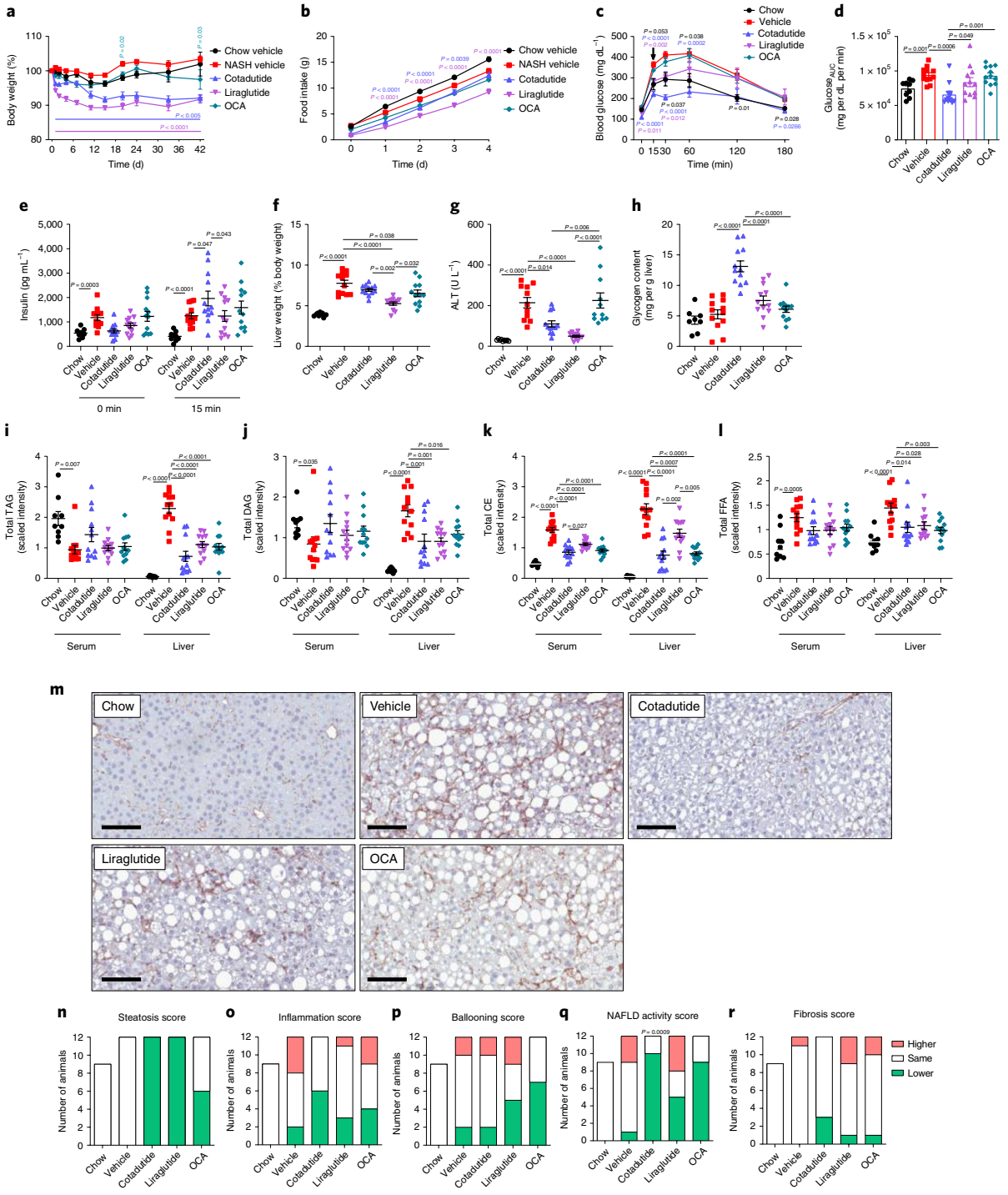

Fig. 6 | Superior efficacy of cotadutide on NASH end points in C57BL6/J mice fed an AMLN diet for 29 weeks, compared with liraglutide and OCA treatment. Effect of sub-chronic cotadutide (10 nmol per kg (body weight), SC, QD for 6 weeks), liraglutide (40 nmol per kg (body weight), SC, QD for 6 weeks) or OCA (70 μmol per kg (body weight), per os, QD for 6 weeks) compared with those in vehicle-treated or lean chow-fed mice. **a**, Body weight expressed as change in body weight from baseline (%). **b**, Cumulative food intake over the first 4 d of dosing. **c**, Blood glucose profile following intraperitoneal injection of 1.5 mg per kg (body weight) glucose after 4 weeks of dosing. **d**, Area under the ipGTT curve. **e**, Plasma insulin levels at 0 and 15 min during GTT. **f**, Terminal liver weight normalized to body weight. **g**, Terminal plasma ALT. **h**, Hepatic glycogen levels. **i**–**l**, Serum and liver levels of total lipid species of triglycerides (TAG) (**i**), diacylglycerols (DAG) (**j**), cholesterol esters (CE) (**k**) and free fatty acids (FFA) (**l**). **m**, Representative type I collagen-stained liver sections. Scale bars, 200 μm. **n**–**r**, Responder rate (number of mice to exhibit improved versus no change versus higher) for steatosis (**n**), inflammation (**o**), ballooning (**p**), NAFLD activity score (NAS) (**q**) and fibrosis (**r**), shown as number of mice per group and evaluated by comparing scores from terminal versus pre-study biopsy liver sections. Chow ($n = 9$); vehicle ($n = 12$); cotadutide ($n = 12$); liraglutide ($n = 12$); OCA ($n = 12$) mice per group. Data are represented as mean ± s.e.m. For statistical analysis in **a**–**c**, comparisons were versus vehicle controls using two-way repeated-measures ANOVA followed by post hoc Dunnett's multiple comparisons test; in **d**–**l**, a two-sided Student's *t*-test was used for chow controls versus vehicle to determine effect of NASH diet and one-way ANOVA with post hoc Tukey's multiple comparison test for treatment effect with the chow group excluded; and in **n**–**q**, comparisons were versus vehicle, using chi-squared test for pairwise comparisons.

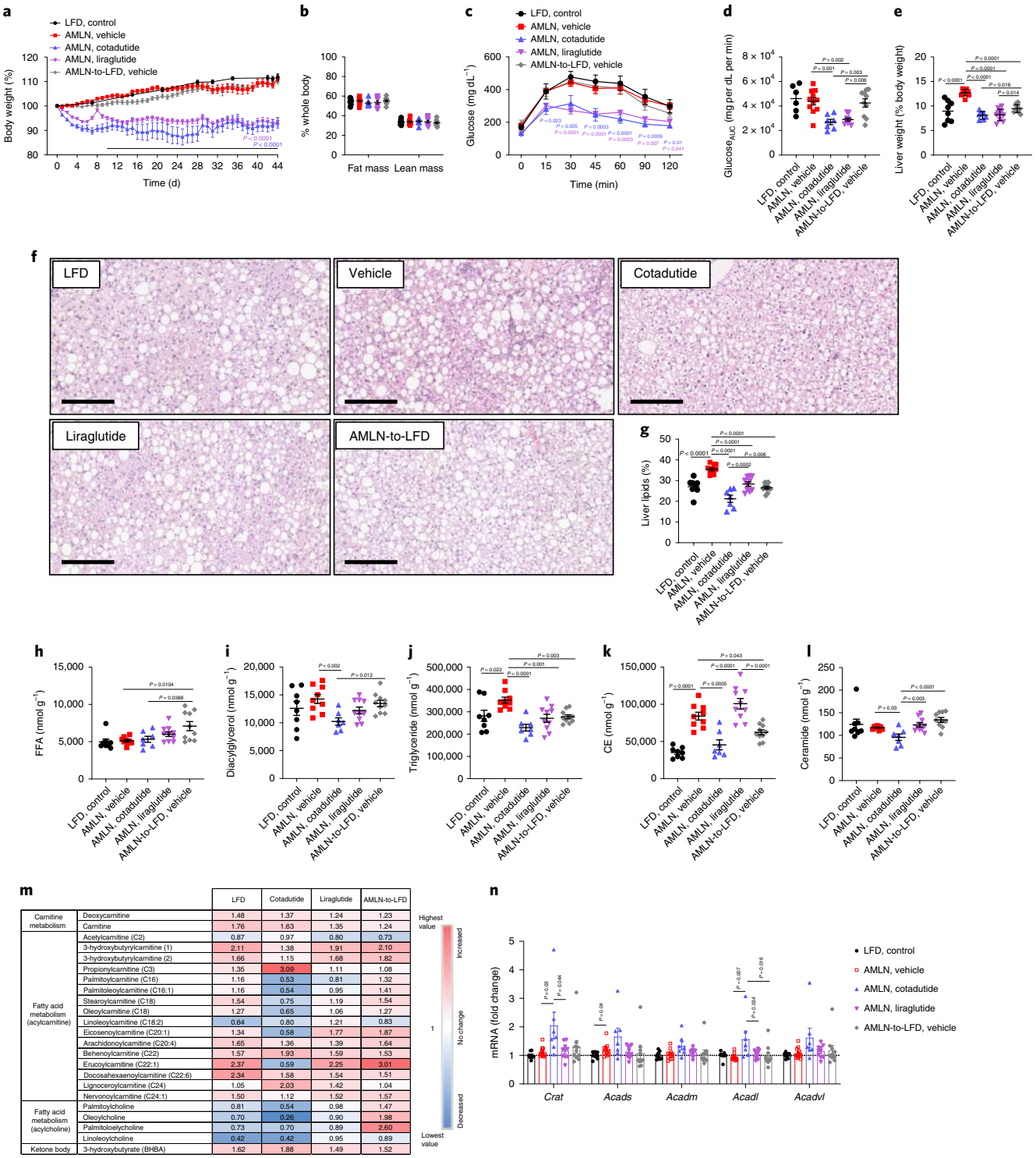

m

		LFD	Cotadutide	Liraglutide	AMLN-to-LFD
Carnitine metabolism	Deoxycarnitine	1.48	1.37	1.24	1.23
	Carnitine	1.76	1.63	1.35	1.24
Fatty acid metabolism (acylcarnitine)	Acetylcarnitine (C2)	0.87	0.97	0.80	0.73
	3-hydroxybutyrylcarnitine (1)	2.11	1.38	1.91	2.10
	3-hydroxybutyrylcarnitine (2)	1.66	1.15	1.68	1.82
	Propionylcarnitine (C3)	1.35	3.09	1.11	1.08
	Palmitoylcarnitine (C16)	1.16	0.53	0.81	1.32
	Palmitoleoylcarnitine (C16:1)	1.16	0.54	0.95	1.41
	Stearoylcarnitine (C18)	1.54	0.75	1.19	1.54
	Oleoylcarnitine (C18)	1.27	0.65	1.06	1.27
	Linoleoylcarnitine (C18:2)	0.64	0.80	1.21	0.83
	Eicosenoylcarnitine (C20:1)	1.34	0.58	1.77	1.87
	Arachidonoylcarnitine (C20:4)	1.65	1.36	1.39	1.64
	Behenoylcarnitine (C22)	1.57	1.93	1.59	1.53
	Erucoylcarnitine (C22:1)	2.37	0.59	2.25	3.01
	Docosahexaenoylcarnitine (C22:6)	2.34	1.58	1.54	1.51
	Lignoceroylcarnitine (C24)	1.05	2.03	1.42	1.04
	Nervonoylcarnitine (C24:1)	1.50	1.12	1.52	1.57
Fatty acid metabolism (acylcholine)	Palmitoylcholine	0.81	0.54	0.98	1.47
	Oleoylcholine	0.70	0.26	0.90	1.98
	Palmitoleoylcholine	0.73	0.70	0.89	2.60
	Linoleoylcholine	0.42	0.42	0.95	0.89
Ketone body	3-hydroxybutyrate (BHBA)	1.62	1.88	1.49	1.52

Fig. 7 | Superior reductions in liver lipids with cotadutide versus liraglutide in an *ob/ob* AMLN mouse model of NASH. Effect of sub-chronic cotadutide (30 nmol per kg (body weight), SC, QD for 6 weeks) or liraglutide (40 nmol per kg (body weight), SC, QD for 6 weeks), or reversion from NASH-inducing diet to LFD (AMLN-to-LFD) in male *ob/ob* AMLN NASH mice compared with untreated *ob/ob* LFD controls and vehicle-treated AMLN NASH mice. **a**, Body weight expressed as change in body weight from baseline (%). **b**, Body composition expressed as percentage lean and fat mass. **c**,**d**, Blood glucose profile following intraperitoneal injection of 1.5 mg per kg (body weight) glucose after 4 weeks of dosing (**c**) and area under the glucose curve (**d**). **e**, Terminal liver weight shown as percentage of body weight. **f**, Representative H&E-stained liver sections. Scale bars, 200 µm. **g**, Terminal percentage liver lipid content. **h**–**l**, Terminal hepatic concentration of free fatty acid (**h**), diacylglycerol (**i**), triglyceride (**j**), cholesterol esters (**k**) and ceramide (**l**). **m**, Hepatic fatty acid metabolism–related metabolite levels relative to those after vehicle treatment. **n**, Hepatic mRNA expression of fatty acid oxidation genes. LFD ($n = 8$); vehicle ($n = 11$); cotadutide ($n = 7$); liraglutide ($n = 10$); AMLN-to-LFD ($n = 10$) mice per group. Data are represented as the mean ± s.e.m. For statistical analysis, in **a** and **c**, a two-way repeated-measures ANOVA followed by post hoc Dunnett's multiple comparisons test was used for comparisons versus vehicle controls; and in **b**, **d**, **e**, **g**–**l** and **n**, a two-sided Student's *t*-test was used for vehicle versus LFD to determine the effect of NASH diet, and a one-way ANOVA with post hoc Tukey's multiple comparison test was used for effect of treatment with the LFD group excluded.

compared with vehicle, but this was highest with cotadutide (Fig. 7m and Supplementary Table 7). Levels of glycolysis and gluconeogenesis pathway metabolites did not differ between groups (Supplementary Fig. 10). Similarly, TCA cycle intermediates were unchanged, except for higher citrate and aconitate in the diet-switch group (Supplementary Fig. 10). Cotadutide also elicited specific changes in hepatic phospholipid, ceramide and glycerolipid moieties versus vehicle control and other treatment groups (Supplementary Table 8a,b). Unique differences in hepatic amino acid levels were mediated by cotadutide; arginine, asparagine and glutamine were reduced following cotadutide treatment compared with vehicle, whereas glutamate and urea increased (Supplementary Table 9).

Hepatic expression of genes involved in fatty acid oxidation tended to be higher in the cotadutide group (Fig. 7n). Furthermore, mice with diet-induced NASH had reduced *Ppargc1a* expression, but sub-chronic treatment with cotadutide restored mRNA levels to those of LFD controls, along with notably increased expression of genes associated with mitochondrial biogenesis and turnover (Supplementary Fig. 11). PCA analysis of the transcriptome revealed separation between treatment groups (Supplementary Fig. 12b). Signatures specific to metabolism, including fatty acid and peroxisomal metabolism, were enriched in LFD controls compared with those treated with vehicle (Supplementary Fig. 12 and Supplementary Table 10). Cotadutide treatment was also associated with enrichment of these pathways in addition to oxidative phosphorylation pathways (Supplementary Fig. 12 and Supplementary Table 10).

Cotadutide resolves hepatic fibrosis and inflammation in *ob/ob* AMLN NASH mice. Hepatic fibrosis was markedly increased in AMLN vehicle mice relative to LFD controls. Cotadutide lowered collagen staining by ~17%, although this was not statistically significant owing to one unresponsive mouse (Fig. 8a,b). Plasma ALT was lowered by cotadutide (Fig. 8c), as was liver α-smooth muscle actin (αSma), Picrosirius red (PSR) and hydroxyproline (Fig. 8d–f and Extended Data Fig. 5). Liraglutide also lowered liver αSma, PSR and hydroxyproline (Fig. 8d–f and Extended Data Fig. 5). NAS was also markedly increased in AMLN vehicle animals relative to LFD controls, and was reduced by cotadutide as well as a LFD switch (Fig. 8g and Extended Data Fig. 6). CD68 scoring, as a marker of immune-cell infiltration, was increased in NASH vehicle mice but was reduced only by cotadutide treatment (Extended Data Fig. 7). The fibrosis stage was higher in AMLN vehicle relative to LFD, and was improved only by cotadutide treatment (Fig. 8h).

Plasma levels of C3M, a neo-epitope fragment of type III collagen cleaved during degradation and circulating levels of P4NP7S, an internal epitope derived from the basement membrane collagen type 4 upon formation, were increased in NASH and reduced only in cotadutide-treated mice (Fig. 8i,j). Levels of pro-C5, a type V collagen pro-peptide marker, were not altered (Fig. 8k).

Biocarta signatures related to inflammation and fibrosis showed marked changes in the Il-12 pathway, Il-17 pathway and type 1 and type 2 helper T-cell pathway in LFD controls and cotadutide compared with NASH vehicle. (Supplementary Fig. 13a and Supplementary Table 10). The Tgfβ Il-4 and Il-6–Jak–Stat3 pathways also tended to be impacted by cotadutide treatment (Supplementary Fig. 13a and Supplementary Table 10). Hallmark apoptosis and inflammatory response signatures were notably enriched in AMLN vehicle animals compared with LFD and cotadutide animals. In addition, the transcriptome following cotadutide treatment was different from that following vehicle for the tumour necrosis factor-α (Tnfα) signalling via nuclear factor κ-light-chain-enhancer of activated B cells (NFκB) pathway (Supplementary Fig. 13b and Supplementary Table 10).

Quantitative PCR analysis confirmed transcriptomic analyses. Furthermore, hepatic transcript levels of collagens (*Col1a1*, *Col3a1*, *Col4a1*), regulators of collagen turnover (*Timp1*, *Mmp9*) and inflammatory mediators (*Il-1b*, *Tgfb*, *Tnf-α*, *Ccl2* and *Cd68*) were all increased in AMLN vehicle compared with LFD controls (Fig. 8l). Cotadutide, liraglutide and diet switching all substantially reduced levels of *Col1a1*, *Col3a1*, *Timp1*, *Ccl2* and *Cd68* relative to those after AMLN vehicle treatment, but cotadutide-treated mice showed the greatest reduction and uniquely reduced *Mmp9*, *Il-1b* and *Tnf* (Fig. 8l).

Discussion

NASH is an unmet medical need, and future therapies will need to resolve NASH features (steatosis, inflammation, hepatocyte ballooning) and either reduce or not worsen hepatic fibrosis. Here, the Glp-1R/GcgR dual agonist, cotadutide (MEDI0382), reduced steatosis, inflammation and fibrosis in two distinct mouse models of NASH, in addition to weight loss, improved glucose homeostasis and endogenous insulin production. Liraglutide, a Glp-1 monoagonist, induced equivalent weight loss; however, hepatic benefits were greater with cotadutide, attributable to additional engagement of GcgR. Cotadutide inhibited hepatic lipogenesis, enhanced mitochondrial turnover and oxidative capacity to levels similar to those induced by monoagonism of GcgR by g1437 (a lipidated/long-acting Gcg agonist), suggesting that this effect was mediated through cotadutide's Gcg component. These pleiotropic effects of cotadutide, and clinical data showing that cotadutide quite effectively reduces liver fat in T2DM[11], suggest that cotadutide may be a viable therapeutic option for the treatment of NAFLD and NASH.

Temporal assessment of endogenous Gcg and hepatic glycogen content showed an inverse relationship to cotadutide exposure levels. Because cotadutide resolved glucose homeostasis, its therapeutic Gcg component more likely suppressed endogenous Gcg rather than changes in glucose per se. Liver glycogen content was rapidly depleted 2 h and 6 h after cotadutide dosing, but then rebounded back above normal at 16 h post dose, inversely proportional to cotadutide pharmacokinetics. A reduction in food intake may partially contribute to a reduction in hepatic glycogen, but treatment with liraglutide matched to result in similar reduced food intake did not change liver glycogen content. Indeed, g1437 elicited similar glycogen depletion without impacting food intake. Therefore, enhanced liver glycogen flux mediated by cotadutide is directly through GcgR signalling. During a hyperglycaemic clamp, fasted cotadutide-treated mice also exhibited increased gluconeogenesis to stabilize glycaemia. Maintenance of pancreatic β-cell function via Glp-1 action allowed the liver to switch to glycogen synthesis upon hyperglycaemia, that was absent in g1437-treated animals. Likewise, metabolites associated with glycogen synthesis and glycogenolysis were correspondingly increased by cotadutide. This physiologic regulation of hepatic glycogen flux likely contributes to the mechanism of improved glucose homeostasis by cotadutide in T2DM[11,13].

A key pathological feature of NAFLD and NASH is excess hepatic lipid accumulation,[3] caused by excess supply of metabolic substrates leading to chronic generation of potential toxic lipid species (for example, ceramides) and increased de novo lipogenesis.[24] Cotadutide effectively reduced the levels of lipotoxic species in NASH mice, and reduced de novo lipogenesis in vivo and in vitro. Numerous Gcg-induced signalling mechanisms related to lipogenesis and lipid-handling pathways were revealed in complementary murine and human hepatocyte phosphoproteomic analyses. Several new sites of phosphorylation on key proteins were identified, some involved in Gcg signalling and negative control of insulin signalling (GcgR, Pka catalytic subunit, Irs1 and Irs2), and others in carbohydrate and lipid metabolism (Acly, Acc2, Gpam, Dgat1) and account for inhibition of hepatic lipogenesis by cotadutide and Gcg. Increased expression of gluconeogenic genes was observed, in line with the Gcg's known activation of Creb via Pka, and subsequent

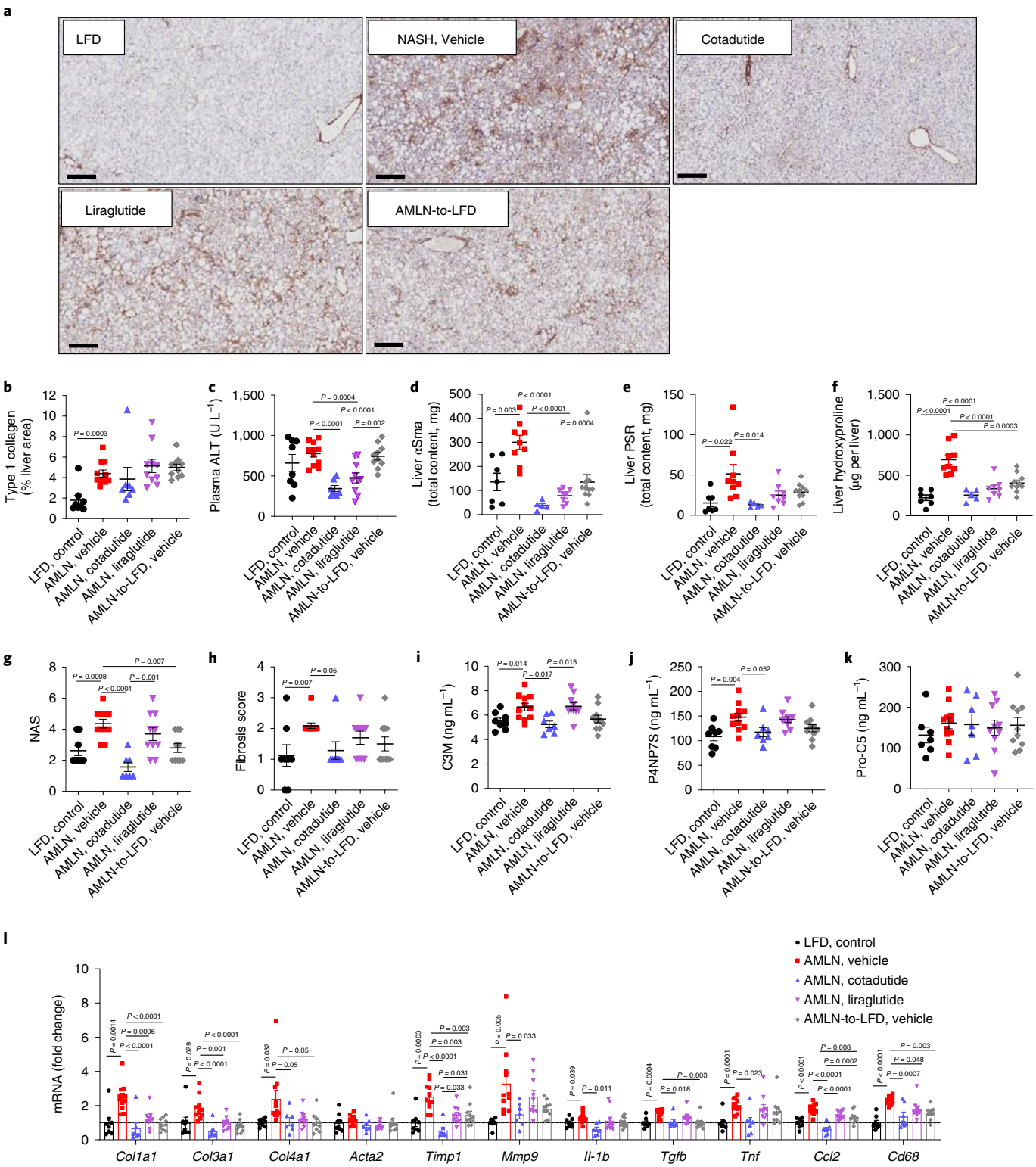

Fig. 8 | Cotadutide further reduces hepatic fibrosis and inflammation compared with that after liraglutide or diet switch in an *ob/ob* AMLN mouse model of NASH. Effect of sub-chronic cotadutide (30 nmol per kg (body weight), SC, QD for 6 weeks), liraglutide (40 nmol per kg (body weight), SC, QD for 6 weeks) or reversion to LFD on fibrosis endpoints from male *ob/ob* NASH mice. **a**, Representative type I collagen-stained liver sections. Scale bars, 200 µm. **b**, Quantification of collagen, type 1 (Col1) staining in **a**. **c**, Plasma ALT levels. **d**, Quantification of αSma staining; representative images are in Supplementary Fig. 14. **e**, Quantification of PSR staining; representative images are in Supplementary Fig. 14. **f**, Liver hydroxyproline content. **g**, NAS. **h**, Fibrosis scores. **i**–**k**, Quantification of plasma levels of C3M, a type III collagen peptide fragment (**i**), P4NP7S, a type IV collagen pro-peptide fragment (**j**) and pro-C5 (**k**). **l**, Hepatic transcript levels of fibrosis- and inflammation-related genes. LFD ($n = 8$); vehicle ($n = 11$); cotadutide ($n = 7$); liraglutide ($n = 10$); AMLN-to-LFD ($n = 10$) mice per group. Data are represented as the mean ± s.e.m. For statistics, a two-sided Student's *t*-test was used for vehicle versus LFD to determine effect of NASH diet, and a one-way ANOVA with post hoc Tukey's multiple comparison test was used to determine treatment effect with the LFD group excluded.

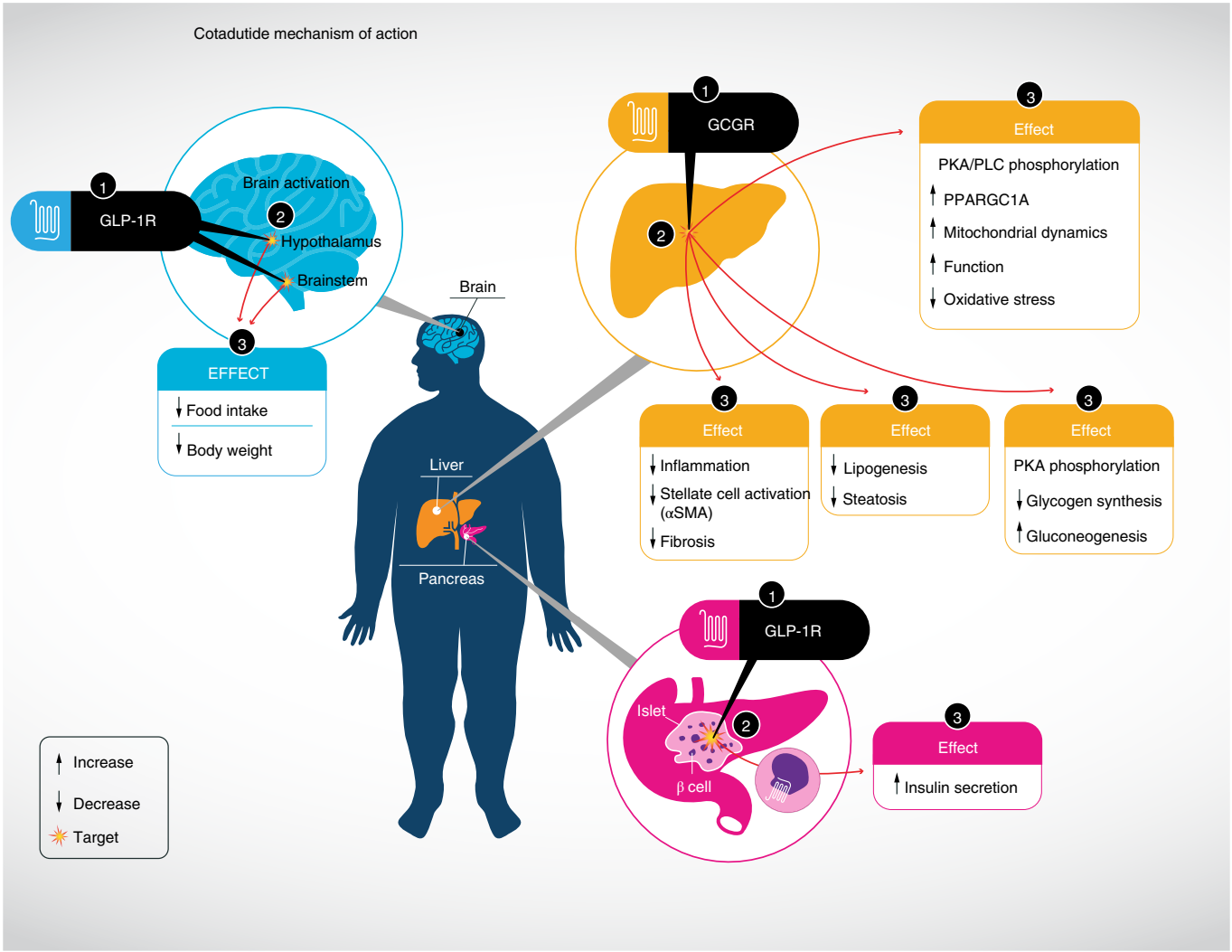

Fig. 9 | Summary of cotadutide mechanism of action at target organs. The dual-agonist activity of cotadutide acts at the GLP-1R in the brain to inhibit appetite resulting in decreased food intake and body weight loss. Meanwhile, the GLP-1R agonist activity at pancreatic β-cells increases insulin secretion to improve whole-body glucose control. Cotadutide also acts at the GCGR of hepatocytes in the liver to improve mitochondrial maintenance and function, leading to lower levels of oxidative stress. GCGR signalling in the liver also decreases de novo lipogenesis and glycogen synthesis, resulting in lower lipid content and a greater flux of glucose through the liver. Altogether, these action in the liver reduces inflammation and stellate cell activation, resulting in less fibrosis, a major hallmark of NASH morbidity and mortality. Although these observations originated from preclinical studies in mouse models of NASH, these effects are being replicated in clinical studies of people with T2DM.

Ppargc1a transcription. Although Ampk phosphorylation may inhibit gluconeogenic gene expression[23,25], it is apparent that the induction of *Ppargc1a* by cotadutide/Gcg over-ruled Ampk in this regard. These findings represent new insight in Gcg action in hepatocytes and unveils mechanisms whereby Gcg halts hepatic anabolic processes (such as lipogenesis) while activating catabolic glycogenolysis, lipolysis and ketogenesis. Specific kinase(s) responsible for some of the novel Gcg-dependent phosphorylations, downstream of Pka, and their functional consequence on regulation of de novo lipogenesis require further experimentation to be elucidated, and alternative signalling mechanisms should not yet be ruled out.

Cotadutide augmented mitochondrial turnover, resulting in an overall more functional mitochondrial population reflected by increased hepatocyte oxidative capacity. This was mediated by the Gcg component of cotadutide as pharmacological inhibition of GcgR signalling blocked both the elevated basal and maximal OCR induced by cotadutide. This improvement in mitochondrial respiration complements in vivo data showing increased oxygen consumption and reduced respiratory exchange ratio in mice treated with cotadutide[13]. Collectively, this indicates that increased energy expenditure along with preferential fat oxidation in vivo is mediated through the enhanced mitochondrial maintenance and function[13]. Moreover, together with cotadutide-induced inhibition of hepatic de novo lipogenesis, this increase in mitochondrial function mediated by cotadutide represents a major mechanism that resolves hepatic steatosis in NASH mice.

The pathogenesis of hepatic fibrosis in the context of NASH is thought to be the result of prolonged inflammation and activation of resident stellate cells to activated, collagen-secreting myofibroblasts. Fibrosis is a key histopathological feature associated with morbidity and mortality in people with NASH[26]. Transcriptional, biochemical and histologic data shown here suggest that cotadutide mitigated hepatic inflammation and improved fibrosis. Indeed, cotadutide administration in the *ob/ob* AMLN NASH model, with the more severe hepatic fibrosis, was associated with reduced hepatic collagen, α-Sma and PSR, hydroxyproline content, circulating collagen markers and suppression or normalization of multiple inflammatory and pro-fibrotic genes. However, neither GcgR nor

Glp-1R is expressed in human Kupffer or stellate cells, suggesting that the anti-inflammatory/anti-fibrotic effects of cotadutide are likely not mediated on these cell types directly. More likely, the reduction in hepatic steatosis and improved mitochondrial function induced by cotadutide, combined with the weight loss and restored glucose homeostasis, precedes, and indirectly leads to, reduced inflammation and less activation of stellate cells, allowing for remodelling and resolution of the extracellular matrix. Regardless, the cotadutide-induced reversal of fibrosis in our preclinical models is unprecedented and supportive of current clinical trials in people with NASH.

Indeed, the combination of metabolic and NASH benefits provided by cotadutide supports its use as a NASH therapy over GLP-1R monoagonist liraglutide or the FXR agonist OCA, two therapies with positive phase 2 clinical data[27,28]. In the liraglutide safety and efficacy in patients with NASH (LEAN) trial, more participants treated with liraglutide versus placebo exhibited resolution of NASH (39% versus 9%, respectively), and also improved fibrosis stage (26% versus 14%).[27] Likewise, in the FXR ligand for non-cirrhotic, non-alcoholic steatohepatitis (FLINT) trial, more people receiving OCA showed a reduction in NAS versus placebo (20% versus 12%, respectively) and fibrosis stage (35% versus 17%); however, other metabolic comorbidities, including obesity and diabetes, were not impacted[29]. In our preclinical model, NAS was reduced in more mice treated with cotadutide (83%), compared with OCA (75%) or liraglutide (42%) and vehicle controls (8%). Further, cotadutide improved fibrosis stage (25% of animals) with no worsening, versus only 8% for each of the OCA and liraglutide groups, with some mice exhibiting worsened fibrosis. Thus, cotadutide appears superior to OCA and liraglutide in this mouse model for NASH resolution and improvement in fibrosis, especially in the context of similar body weight loss to that observed with liraglutide. Furthermore, in the more severe *ob/ob* AMLN NASH model, fibrosis was resolved in all but one of the cotadutide-treated mice and was associated with improved NAS versus other treatment arms, again in the context of equivalent weight loss. These results underscore the potential impact of cotadutide with its pleiotropic mechanisms of action not only on NASH hepatopathology, but also on metabolic comorbidities. This is in contrast to more focused hepatic targeting approaches to treat only NASH[28], whereby combination with other therapeutics will likely be needed to address the wider metabolic disease state.

In summary, in characterizing cotadutide effects in the liver, we have gained new mechanistic insight into the pathogenesis of NAFLD/NASH. The dual Glp-1R/GcgR action of cotadutide positively impacts key metabolic and pathological components of NASH in part through mitigating features that drive hepatocellular injury including nutrient oversupply, toxic lipid species generation, mitochondrial dysfunction and, importantly, fibrosis (Fig. 9). These effects are unique to the dual action of cotadutide, as Glp-1 alone produced only modest hepatoprotective effects, despite similar weight loss and glycaemic control. As such, cotadutide represents a promising distinctive therapeutic approach for people with obesity and/or T2DM with NAFLD/NASH comorbidities.

Methods

Animal studies. Animal studies were approved by either the Institutional Animal Care and Use Committee at MedImmune/AstraZeneca or Vanderbilt University in accordance with Animal Welfare Act guidelines, or Gubra under personal licenses issued by the Danish Committee for Animal Research. Details regarding power calculations and sample size selection are included in the Reporting Summary. Animals were housed in standard caging at 22 °C on a 12-h light–dark cycle.

GLP-1R KO study. Male GLP-1R KO mice and C57Bl/6J WT littermates (Jackson Laboratories), 7–10 weeks of age, were maintained on 60% HFD (D12492; Research Diets) for 8 weeks to establish obesity. Mice were then switched to 45% HFD (D12451; Research Diets) for ease of food intake measurements and were acclimated to the new diet for 2 weeks. Mice were randomized to drug treatment groups ($n = 7–9$) on the basis of body weight and then were administered vehicle (50 mM phosphate buffer, propylene glycol (1.85% wt/vol), 0.04% PS-80, pH 7.5), cotadutide (10 nmol per kg (body weight)), liraglutide (10 nmol per kg (body weight)), g1437 (10 nmol per kg (body weight)) or a combination of liraglutide+g1437 (5+5 nmol per kg (body weight)). Vehicle and test agents were administered subcutaneously once daily for 14 d. An intraperitoneal glucose tolerance test was performed on day 12 after a 4 h fast (1.25 g glucose per kg (body weight)), and body composition was measured by magnetic resonance imaging on day 14.

Cotadutide time course study in DIO C57Bl/6J. To understand the temporal effects associated with cotadutide treatment, a separate study utilizing 20-week old C57Bl/6J DIO male mice (Jackson Laboratories) was performed. Animals were dosed with vehicle or cotadutide (10 nmol per kg (body weight)), liraglutide (10 nmol per kg (body weight)), g1437 (10 nmol per kg (body weight)) or a combination of liraglutide+g1437 (5+5 nmol per kg (body weight)) 2 h prior to lights out at 16:00, for 6 consecutive d. On the seventh day, animals were euthanized at time 0, or received a final dose and euthanized at 2, 6 or 16 h post final dose ($n = 4$ mice per group per time point). Blood was collected via cardiac puncture, and livers were excised, weighed and processed for further analysis. All animals had ad libitum access to food for the study entirety. This study is a replication of a separate study consisting of only vehicle- and cotadutide-treated mice presented in Supplementary Fig. 2.

Hyperglycaemic clamp and stable-isotope infusions in DIO C57Bl6J mice. This study used carbohydrate and lipid tracing, with radio-labelled glucose and water, in a single animal under clamp conditions. Mice were maintained on a modified light–dark cycle such that light cycle was between midnight and noon to allow for appropriately timed dosing and subsequent clamp experiment. Twenty-week old C57Bl/6J DIO male mice (Jackson Laboratories) were dosed with vehicle or cotadutide (10 nmol per kg (body weight)), liraglutide (10 nmol per kg (body weight)) or g1437 (10 nmol per kg (body weight)) 2 h prior to lights out at 10:00 for 6 consecutive d ($n = 8–10$). Five days prior to the clamp, mice underwent arterial and venous catheterization[30–32]. On the seventh day of treatment, animals were fasted for 5 h (starting at 9:00) and received a final dose at 10:00 (Fig. 3a). After 3 h of fasting, an arterial blood sample was obtained to determine natural isotopic enrichment of plasma glucose. Immediately following this sample, a quantitative stable-isotope delivery to increase isotopic enrichment above natural isotopic labelling was initiated[33]. A [6,6-$^2H_2$]glucose-^2H_2O (99.9%)-saline bolus was infused for 25 min to enrich total body water to 4.5% and provide a glucose prime (80 mg kg^{-1}) ($t = –120$ min to –95 min). A continuous infusion of [6,6-$^2H_2$]glucose ($t = –95$ min to 0 min; 0.8 mg kg^{-1} min^{-1}) was started following the [6,6-$^2H_2$]glucose-^2H_2O-saline prime. The hyperglycaemic clamp was initiated at $t = 0$ min with a variable infusion of glucose ((50% dextrose + ^2H_2O (0.04 mol% excess (MPE)) + [6,6-$^2H_2$] glucose (0.08 MPE))), to induce stable hyperglycaemia (250–300 mg dL^{-1}) and stable enrichment of ^2H_2O and [6,6-$^2H_2$]glucose in plasma. Arterial glucose levels were monitored every 10 min to provide feedback for adjustment of the glucose-infusion rate (GIR). Steady-state blood sampling for glucose kinetics was performed at –10 and +90–120 min of hyperglycaemia. Red blood cells were continuously infused during the hyperglycaemic period to maintain haematocrit. At $t = 120$ min, mice were euthanized, and liver tissue was immediately frozen in liquid nitrogen. The experimental design is presented in Fig. 3a. Stable isotopes were purchased from Cambridge Isotope Laboratories. Each infusate was prepared in a 4.5% ^2H_2O-enriched saline solution.

Plasma glucose enrichments ([6,6-$^2H_2$]glucose), isotopomer distribution and the enrichment ratio of deuterium on the fifth (C5) and second carbon (C2) of glucose were assessed by gas chromatography–mass spectrometry (GC–MS)[34,35]. Each plasma sample collected during the study was chemically derivatized so as to obtain di-*O*-isopropylidene propionate, aldonitrile pentapropionate and methyloxime pentapropionate derivatives of glucose.

Liver glycogen was digested by amyloglucosidase[36], and glucose mass and enrichments were assessed in the homogenate in the same manner. To determine ^2H_2O in plasma, the sample was spiked with acetone and NaOH. After exchange, ^2H-enriched acetone is extracted with chloroform and assayed by GC–MS[37]. Hepatic palmitate and glyceride enrichments and content were assessed in saponified extracts spiked with internal standards (1,1,2,3,3-[$^2H_2$]glycerol and heptadecanoic acid)[32,38]. Glucose fluxes were assessed using non-steady-state equations (volume of distribution of glucose = 130 mL per kg (body weight))[31]. The contribution of gluconeogenesis was assessed as the ratio of C5 and C2 of plasma glucose[39,40]. Direct hepatic glycogen synthesis ([6,6-$^2H_2$]glucose in glycogen = liver glycogen mass (mg g^{-1}) × (glycogen [6,6-$^2H_2$]glucose MPE/plasma [6,6-$^2H_2$]glucose MPE)) from plasma glucose and percent indirect hepatic glycogen synthesis (C5/C2 in liver glycogen × 100) from gluconeogenesis were calculated. Simultaneously, hepatic de novo lipogenesis and triglyceride esterification rates were calculated from the incorporation of ^2H in palmitate and glyceride, respectively. The contribution of newly synthesized palmitate and esterified glycerol was determined using the following equations:

Percentage newly made palmitate = palmitate M+1 MPE/(plasma ^2H_2O MPE × n) × 100, where n represents the number of exchangeable hydrogens, which was assumed to be 22 (ref. [32]).

Percentage newly made esterified glycerol = (glycerol M+1 enrichment MPE + 2 × M+2 enrichment MPE)/(plasma ^2H_2O MPE × 4.25) × 100, where n represents the number of exchangeable hydrogens, which was assumed to be 4.25 (ref. [32]).

Sub-chronic dosing in C57Bl/6J NASH model. In a separate study, male C57BL/6J mice aged ~6 weeks (Janvier Labs) were maintained on chow (Altromin 1324) or high trans-fat, high-fructose and high-cholesterol (AMLN) diet (D09100301; Research Diets) for 29 weeks prior to study start to establish a severe NASH phenotype. Three weeks prior to study start, mice were subjected to a liver biopsy procedure[41] for baseline NASH phenotype measurements. After an overnight fast, a small incision in the midline of the mouse under isoflurane anaesthesia was made and the left lateral lobe of the liver was exposed. A cone shaped wedge of liver tissue (~50–100 mg) was excised from the distal portion of the lobe, weighed and fixed in 4% paraformaldehyde. The cut surface of the liver was instantly electrocoagulated using bipolar coagulation. The liver was returned to the abdominal cavity, and the abdominal wall was sutured and the skin closed with staples. Three weeks post-biopsy, mice were randomized to treatment arms on the basis of body weight, liver fibrosis and steatosis scores. Mice on AMLN diet (n = 12 per group) were administered vehicle (50 mM phosphate buffer, propylene glycol (1.85% wt/vol), 0.04% PS-80, pH 7.5, n = 11), cotadutide (10 nmol per kg (body weight)) or liraglutide (40 nmol per kg (body weight)) via subcutaneous injection once daily just prior to lights off. Another group was administered Obeticholic acid (OCA; Selleckchem, Houston, TX) dosed at 70 µmol per kg orally once daily. The OCA group received an additional subcutaneous vehicle injection, and the vehicle, cotadutide and liraglutide groups received an oral dose of vehicle (0.5% carboxymethyl cellulose) at the same time; thus, all mice received two daily administrations of vehicle or test agent. Treatment and diet were continued for 6 weeks. Body weight was recorded daily. An intraperitoneal glucose tolerance test was performed on day 28 after a 4-h fast (1.5 g glucose per kg (body weight)), with blood glucose sampled from tail vein collections (BIOSEN c-Line glucose meter; EKF-diagnostics). On study day 42, mice were euthanized via isoflurane overdose, and cardiac blood was collected for terminal analyses. Liver was excised, weighed and prepared for downstream analyses.

Sub-chronic dosing in *Ob/Ob* NASH model. Male *Lep^{ob}Lep^{ob}* mice with C57Bl/6J background (B6.Cg-Lepob/J, Jackson Laboratories), aged 8 weeks were placed on either low-fat control diet (LFD; D09100304, Research Diets) or AMLN diet (D09100301, Research Diets) for 8 weeks. On day −3, mice on AMLN diet were randomized to drug treatment groups on the basis of body weight, non-fasting blood glucose (Breeze2 glucometer), and plasma ALT (Cobas c-111, Roche Diagnostics) from retro-orbital blood collection in the conscious mouse. Mice on LFD (n = 8) were not administered any vehicle or compound. Mice on AMLN diet were administered vehicle (50 mM phosphate buffer, propylene glycol (1.85% wt/vol), 0.04% PS-80, pH 7.5, n = 11), cotadutide (n = 7), liraglutide (n = 10) or switched back to LFD (AMLN-to-LFD) and administered vehicle (n = 10). Vehicle and test agents were administered subcutaneously once daily for 6 weeks. Cotadutide and liraglutide dose started at 10 nmol per kg (body weight) and escalated by 10 nmol per kg (body weight) every 2 days until the target dose of 40 nmol per kg (body weight) was achieved (3 steps). For cotadutide, after 4 d at 40 nmol per kg (body weight), the dose was lowered to 30 nmol per kg (body weight) for the remainder of the study in order to match body weight loss between cotadutide and liraglutide treatment arms. Body weight was measured daily. Non-fasted blood glucose was recorded on day 0 and weekly thereafter for all mice (Breeze2 glucometer). An intraperitoneal glucose tolerance test was performed on day 28 after a 4h fast (1.5 g per kg (body weight) glucose). Vehicle or drug was administered for 6 weeks at which point mice were euthanized in the non-fasted state, and blood was collected via cardiac puncture and livers excised, weighed and processed for further analysis.

Plasma measurements. *ALT.* Terminal blood was collected in EDTA-coated tubes and centrifuged at 10,000*g* for 10 min. The plasma was collected and analysed for ALT levels using a biochemistry analyser (Cobas c-111, Roche Diagnostics).

Plasma collagen fragment analysis. Enzyme-linked immunosorbent assay (ELISA)-based techniques for the detection of C3M, P4NP7S and C5M in plasma were conducted as described below[42–44].

For C3M, a 96-well streptavidin-coated plate (Roche Diagnostics) was further coated with 5 ng mL^{-1} of the synthetic biotinylated peptide KNGETGPQGP–biotin dissolved in PBS–TBE buffer at 20 °C for 30 min with constant shaking at 300 r.p.m. After being washed 5 times in wash buffer, 20 µL of the sample was added followed by 100 µL of peroxidase-conjugated anti-human monoclonal antibody-NB51-32 CO3-610 solution (23 pg mL^{-1} in incubation buffer). The plate was incubated for 1 h at 20 °C with shaking at 300 r.p.m. Following an additional five washes, 100 µL of tetramethylbenzinidine (TMB) (Kem-En-Tec cat. no. 438OH) was added. The plate was incubated for an additional 15 min in the dark with shaking at 300 r.p.m. The reaction was stopped upon the addition of 100 µL of stopping solution (95–97% H2SO4, Merck cat. no. 1.00731). The plate was analysed at 450 nm with 650 nm as the reference (Molecular Devices).

For P4NP7S, a 96-well streptavidin-coated plate (Roche Diagnostics) was further coated with the biotinylated peptide biotin–PGEILGHVPG dissolved in assay buffer (50 mM Tris-BTB, pH 7.4), incubated for 30 min at 20 °C in the dark and subsequently washed in wash buffer (20 mM Tris, 50 mM NaCl, pH 7.2). Then, 20 µL of the peptide calibrator or sample were added to appropriate wells, followed by 100 µL of HRP-conjugated monoclonal antibody NB102-1E6. The plate was incubated for 1 h at 20 °C and then washed. After the addition of 100 µL of tetramethylbenzinidine (TMB) (Kem-En-Tec cat. no. 438OH), the plate was incubated for an additional 15 min at 20 °C. The reaction was stopped upon the addition of 100 µL of stopping solution (1% H_2SO_4). The plate was analysed at 450 nm with 650 nm as the reference (Molecular Devices).

For C5M, a 96-well streptavidin-coated plate (Roche Diagnostics) was coated with 2.5 ng of the biotinylated synthetic peptide, TAALGDIMGHGGC–biotin, dissolved in assay buffer (50 mM Tris, 1% bovine serum albumin (BSA), 0.1% Tween-20, adjusted to pH 7.4 at 20 °C) and incubated for 30 min at 20 °C. First, 20 µL of the peptide calibrator or sample were added to appropriate wells followed by 100 µL of 125 ng conjugated monoclonal antibody. The plate was incubated for 1 h at 20 °C and then 100 µL tetramethyl benzinidine (TMB) (Kem-En-Tec cat. no. 438OH) was added, followed by an additional 15 min incubation at 20 °C in the dark. After each incubation step, the plate was washed five times in washing buffer (20 mM Tris, 50 mM NaCl, pH 7.2). The TMB reaction was stopped upon the addition of 100 µL of stopping solution (1% HCl). The plate was measured at 450 nm with 650 nm as the reference (Molecular Devices).

Plasma insulin. Mouse/rat insulin kit (MSD) was used as per kit instructions.

Plasma glucagon. Glucagon R-plex kit (MSD) was used as per kit instructions.

GLP-1R and GCGR Bioassay. Serum peptide content was determined using a cell-based cAMP accumulation bioassay (Cisbio) to estimate peptide bioactivity in serum samples at hGLP1-R or hGCGR.[45] CHO K1 cells stably transfected with human GLP-1R or human GCGR were used to determine apparent peptide concentration in serum from treated animals by comparing potency for inducing cAMP accumulation. Reference peptides at a known concentration were spiked into naive serum to create standard curves. Bioactivity data were analysed using nonlinear regression analysis in GraphPad Prism.

Liver lipid quantification. Total lipids were measured in liver samples using a Bruker LF-90 minispec system (Bruker Biospin Corporation). The data are expressed as the percent lipid relative to the total tissue mass.

Glycogen quantification. Liver and muscle glycogen were measured following tissue lysis, precipitation, digestion and glucose quantification. Tissue was lysed in 0.75% SDS, an aliquot was reserved for protein measurements, and protein in remaining lysate was precipitated upon addition of 100% TCA. Following protein precipitation, supernatant was removed and added to 2.5 volumes of 100% ethanol to precipitate glycogen. After overnight storage at -80 °C, pelleted glycogen samples were washed with 75% ethanol, and dried under speed-vac, followed by digestion with glucoamylase for 1.5 h at 45 °C. Glucose was measured using the glucose oxidase/peroxidase method and read on a Spectramax plate reader (Molecular Devices) at 405 nm.

Histological analysis and quantification of liver tissue. Livers were fixed in 10% neutral-buffered formalin for 24 h. Paraffin-embedded tissue sections were de-paraffinated in xylene and rehydrated in series of graded ethanol. Slides were incubated in Mayer's haematoxylin (Dako), washed in tap water, stained in eosin Y solution (Sigma), hydrated and mounted with Pertex. For Picrosirius red, the slides were incubated in Weigert's iron haematoxylin (Sigma), washed in tap water, stained in Picro-sirius red (Sigma) and washed twice in acidified water. Excess water is removed by shaking the slides and then dehydrated in three changes of 100% ethanol, cleared in xylene and mounted with Pertex.

Histological assessments were conducted by a pathologist under blinded conditions. A modified scoring system, based on the Brunt and Kleiner NAFLD activity score[46], previously developed and validated to enable a more reproducible and semiquantitative assessment of murine liver was used to quantify various parameters of liver phenotype including inflammation, steatosis, hepatocyte ballooning and biliary hyperplasia.

Immunohistochemistry. Immunohistochemistry was performed using a Ventana Discovery ULTRA Staining Module (Ventana Medical Systems). Formalin-fixed, paraffin-embedded liver sections were stained with anti-collagen type 1 (1310-01, Southern Biotech), anti-α-smooth muscle actin (ab124964, Abcam) or anti-CD68 (ab125212, Abcam). Specific antibody details can be found in the Reporting Summary.

Liver hydroxyproline content. Liver samples were homogenized in 6 M HCl and hydrolysed to degrade collagen. Samples were centrifuged and hydroxyproline

content was measured using a colorimetric assay (Quickzyme Biosciences), according to the manufacturer's instructions.

Primary hepatocyte isolation. Primary hepatocytes were isolated using a modified two-step non-recirculating perfusion method.[47] Mice were anaesthetised with isoflurane and the portal vein was cannulated using a 23-gauge needle and a 2 mL min^{-1} flow of HBSS with 5 mM glucose, 0.5 mM EGTA, 25 mM HEPES pH 7.4. Upon blanching of the liver nearly immediately after cannula insertion into the portal vein (a confirmation of successful cannulation), the inferior vena cava (IVC) was cut and the flow rate was increased from 2 mL min^{-1} to 8 mL min^{-1}. Approximately 50 mL of HBSS was perfused through the liver, taking approximately 6 min. During this time, the IVC was periodically clamped for 5-s periods. Digestion medium (low-glucose DMEM (Gibco, Thermo Fisher)), supplemented with 15 mM HEPES, 100 U mL^{-1} penicillin and 0.1 mg mL^{-1} streptomycin (pen/strep), and 100 U mL^{-1} type IV collagenase (Worthington Biochemical Corp) was then perfused at 8 mL min^{-1} for approximately 8 min, or until the liver was fully digested. The IVC was periodically clamped, as before, to accelerate digestion and maximize total cell yield. Total digestion was confirmed upon loss of liver elasticity/ minimal change in liver size upon IVC clamping. The digested liver was excised and transferred to a culture dish containing 15 mL of the digestion medium and was gently ripped and shaken using forceps to release the cells. The cells were gently pipetted up and down three times and then filtered through a 74-µM fine mesh strainer (Dual Manufacturing). The cells were spun at 50*g* for 2 min at 4 °C followed by three washes with 25 mL ice-cold isolation medium (high-glucose DMEM (Gibco, Thermo Fisher) supplemented with 1 mM sodium lactate, 2 mM L-glutamine, 15 mM HEPES, 0.1 µM dexamethasone, 1× pen/strep, and 10% FBS). After the final wash, the hepatocytes were resuspended in 25 mL of isolation medium and the viability and yield were assessed. An aliquot of the cell suspension was mixed in a 4:1 ratio with 0.4% trypan blue, after which the viable hepatocytes were counted using a hemocytometer. The hepatocytes were diluted to 300,000 cells mL^{-1}, and approximately 3 million hepatocytes were seeded per type I collagen-coated plate unless otherwise noted. After a 1-h incubation at 37 °C in a humidified 5% CO_2 incubator, the cells were washed and fresh isolation medium was added for an additional 4 h. Following this initial recovery period, the medium was changed to a serum-free culture medium (low-glucose DMEM (Gibco, Thermo Fisher) supplemented with 10 mM sodium lactate, 2 mM L-glutamine, 5 mM HEPES, 10 nM dexamethasone and 1× pen/strep).

All assays were carried out within 18–24 h post-plating. Hepatocytes were treated for 2–4 h with 100 nM of cotadutide, liraglutide or g1437. Live-cell imaging of hepatocytes stained with Mitotracker Green and Lysotracker Deep Red (Thermo Fisher) was performed using the Leica SP5 X confocal microscope and quantified using the Arivis Vision4D software. In indicated assays, cells were treated with PKA inhibitor, H89 (10 µM, Sigma); AMPK inhibitor, compound C (20 µM, Calbiochem); p38MAPK inhibitor, SB 203580 (20 µM, Calbiochem); PLC inhibitor, U73122 (10 µM, Calbiochem); mTOR inhibitor, rapamycin (1 µM, Sigma); PI3K inhibitor, LY-294 (10 µM, Sigma) or MAPKK inhibitor, PH 98 (20 µM, Sigma).

Human hepatocytes. Human primary hepatocytes were obtained from Samsara Sciences. They were plated on type I collagen-coated plates and cultured in Hepatocyte Maintenance Media (HMM, CC-3197, Lonza) supplemented with Singlequots (CC-4192, Lonza). The components of the Singlequots kit are dexamethasone, insulin and gentamicin/amphotericin B. The cells were cultured for no more than 36 h. For gene expression analyses, hepatocytes were treated for 4 h with the indicated compounds followed by RNA isolation using TRIzol (Life Technologies).

Lipogenesis. De novo lipogenesis was assessed in primary hepatocytes isolated from C57Bl/6J male mice. Hepatocytes were serum-starved overnight, then high-glucose DMEM containing 10 µM cold acetate and 1.0 µCi [^{3}H]acetate (Perkin Elmer) per well of a 12-well plate was added. After a 2-h incubation, hepatocytes were washed with PBS then scraped in 0.1 N HCl. Lipids were extracted by addition of 2:1 chloroform:methanol (vol/vol). After addition of water, samples were centrifuged, and the lower phase was transferred to a scintillation vial containing scintillation fluid. ^{3}H activity was measured using a scintillation counter (Beckman Coulter).

Mitochondrial oxygen consumption. Mitochondrial oxygen consumption was measured using the Seahorse Xfe96 Analyzer (Agilent). Primary mouse hepatocytes were plated at a density of 7500 cells per well and allowed to recover overnight. The medium was exchanged (DMEM containing 5 mM glucose, 4 mM L-glutamine, 2 mM sodium pyruvate, pH 7.4) and the plate was placed in a CO_2-free incubator for 30 min prior to being placed in the analyser. The following compounds were used in the mitochondrial stress test: 1 µM oligomycin (Sigma), 0.5 µM FCCP (Sigma) and 5 µM antimycin A (Sigma). Basal and maximal OCRs were normalized to citrate synthase activity (CSA) (cat. no. K13, Biovision) as a measure of mitochondrial mass.

Liquid chromatography–tandem mass spectrometry: metabolomics. Frozen liver samples were placed in CK14 Precellys tubes for soft tissue and extracted with 1 mL per 100 mg of cold acetonitrile/methanol/water 40/40/20 vol/vol/vol. Homogenization was performed using 3 cycles (30 s per cycle) of 4,000 r.p.m. in a pre-cooled Precellys-24 system with Cryolys unit. A 60-s pause between cycles was used to ensure samples remained cold. After centrifugation at 21,100*g* (14,800 r.p.m.) to pellet debris, supernatants were transferred to 1.5-mL Eppendorf tubes and stored at −80 °C. Prior to analysis, 10 µL of each sample was mixed with 90 µL of ultrapure water and transferred to a 0.3 mL polypropylene HPLC microvial for liquid chromatography–tandem MS (LC–MS/MS) analysis.

Samples were analysed using an LC–MS platform consisting of an Ultimate 3000 chromatography system (Thermo, UK) coupled to an AB4000 triple quadrupole mass spectrometer (ABSciex). The mass spectrometer was operated in negative-ion mode. Chromatographic separation was achieved with a Waters Acquity HSS T3 column, C18 100 × 2.1 mm, 1.8-µm particle size. The column oven housing the analytical column was maintained at a constant temperature of 60 °C. Solvent flow was delivered at 400 µL min^{-1} and buffer composition was as follows: buffer A: 10 mM tributylamine (TBA), 15 mM acetic acid in high-performance LC–MS-grade ultrapure water; Buffer B: 80% (vol/vol) methanol, 20% (vol/vol) isopropanol. Full details of the mass spectrometry method are given in Michopoulos et al.[48].

Raw data were analysed, and peak integration performed with the software package MultiQuant v.2.0.2 (Applied Biosystems/MDS Sciex). Peak areas were exported into Microsoft Excel for normalization and further data processing (*F*-test, *t*-test, fold change). Analytical reproducibility was deemed to be acceptable for those metabolite peaks for which a coefficient of variation of less than 30% was calculated. Metabolite perturbation was considered significant for *t*-test $P < 0.05$, and an average difference greater than 30%.

RNA isolation and real-time PCR. Total liver RNA and genomic DNA were isolated using standard procedures. Qiagen RNeasy columns (Qiagen) were used for RNA purification according to the manufacturer's protocol, including an on-column DNA digestion using DNase I. Equal amounts of RNA were reverse transcribed to complementary DNA using SuperScript III First Strand cDNA synthesis kit (Invitrogen) according to the manufacturer's instructions. Real-Time PCR was performed on a QuantStudio-7 Flex System (Applied Biosystems) using Applied Biosystems TaqMan Fast Universal PCR Master Mix and TaqMan probes. Each sample was assayed in triplicate and quantified using the $-\Delta\Delta CT$ method normalized to endogenous control *Ppia*. Relative gene expression was normalized to a value of 1 for the control group.

RNA sequencing. Total RNA samples treated with RNase-free DNase I (Qiagen) were quantified and analysed using Nanodrop-1000 spectrophotometer (Thermo Fisher) and 2100 Bioanalyzer (Agilent).

RNA sequencing (RNA-seq) libraries were prepared using Illumina TruSeq RNA Library Prep Kit v2 according to the manufacturer's instructions (Illumina). Briefly, poly(A)-containing mRNA in 150 ng total RNA was converted into a double-stranded cDNA library, which was, in turn, ligated to TruSeq paired-end adapters containing unique index barcode sequences. The ligated products were purified and enriched with 15 cycles of PCR. The size distribution of the RNA-seq libraries was analysed on a 2100 Bioanalyzer (Agilent), and the library concentrations were determined using Kapa Library Quantification kit (Kapa Biosystems). Sequencing libraries were normalized and pooled to 4 nM in 10 mM Tris-HCl, pH 8.0 and subjected to denaturation in 0.1 N NaOH for 5 min prior to the final dilution to 1.8 pM. Denatured and diluted libraries were loaded onto NextSeq 500/550 v2 flow cells and paired-end sequencing (2 × 75 cycles) was performed on NextSeq 500 sequencing instruments (Illumina).

Analysis of RNA-seq data. NextSeq data was demultiplexed using bcl2fastq (Illumina). Sequencing reads were aligned to the GRCm38/mm10 mouse assembly by applying STAR v2.5 (Spliced Transcripts Alignment to a Reference)[49]. Reads were counted with RSEM v1.2 (RNA-Seq by Expectation Maximization), and a $\log_2$(transcripts per million) data matrix was generated for further analysis. All samples were confirmed to have at least 30 million unique paired reads, and alignment rates of greater than 79%. Differential expression of genes was determined by linear regression using the limma package in R. *P* values were determined by the eBayes function (Empirical Bayes Statistics), and a Benjamini–Hochberg correction was applied to adjust *P* values for multiple testing.

Analysis of genomic signatures. Data analysis was performed with the R programming language (v.3.4) in R Studio (v.1.0). Genomic signatures were obtained from the public MSigDB database, including Hallmark and Biocarta signatures[50–52]. Details of the selected signatures are listed in Supplementary Tables 5, 6 and 11. Signature scores were calculated for each subject using gene set variation analysis and visualized using the pheatmap package for R[53,54]. Genomic signatures scores were analysed by ANOVA to determine differential response, and adjusted *P* values were calculated by applying Tukey honest significant difference.

Phosphoproteomics analyses. *Mouse hepatocytes.* Cell pellets were lysed by probe sonication for 2 × 20 s (40% amplitude) on ice in 0.5 mL ice-cold 0.1 M Na_2CO_3, pH 11 with protease (cOmplete Protease Inhibitor, Sigma) and phosphatase inhibitors (PhosSTOP, Sigma) + 10 mM sodium pervanadate using a Q125 probe

sonicator (Qsonica). After sonication, the samples were incubated at 4 °C for 1 h, then ultracentrifuged at 100,000*g* for 90 min and the supernatant stored at −20 °C pending analysis. The pellet was washed/re-dissolved gently with 500 µL of 500 mM triethyl ammonium bicarbonate (TEAB; pH 8) and centrifuged at 14,000*g* for 30 min at 4 °C. The supernatant was discarded and the pellet (membrane-enriched fraction) re-dissolved in 6 M urea/2 M thiourea, 10 mM DTT and 1 µL (4 µg) endoproteinase Lys-C (Vako Chemicals) and incubated at room temperature for 2 h. After incubation, the cysteines were alkylated using 20 mM iodoacetamide for 30 min in the dark, then the solution was diluted 10 times with 20 mM TEAB; pH 7.8 with trypsin added (2–5%) and incubated at room temperature overnight.

For the soluble proteins, the volume was reduced by centrifugation to 50 µL using a 10-kDa cutoff spin filter (Amicon Ultra, Merck Millipore) at 4 °C. The proteins were washed in 450 µL of 50 mM TEAB, pH 7.8 containing phosphatase inhibitors (PhosSTOP) + 10 mM sodium pervanadate on the filter. After washing, a total of 50 µL 6 M urea/2 M thiourea, 10 mM DTT was added and incubated for 30 min at room temperature. Iodoacetamide was then added to a final concentration of 20 mM and incubated in the dark for 30 min at room temperature. After, 300 µL of 50 mM TEAB, pH 7.8 containing phosphatase inhibitors (PhosSTOP) + 10 mM sodium pervanadate was added, and the solution was centrifuged to reduce the volume to 50 µL. After centrifugation, 150 µL of 50 mM TEAB, pH 7.8 containing trypsin (5 µg) was added to each sample and incubated overnight at room temperature. Concentration of peptides was measured for both the soluble and membranous samples using the Qubit fluorescent technology (Thermo Fisher).

A total of 120 µg peptides for all samples were labelled with TMT10 plex (Thermo Fisher) according to the manufacturer's protocol, resulting in one TMT10 plex for the soluble fraction and one TMT10 plex for the membrane fraction. The control (non-stimulated) samples were labelled with TMT 126, 127N, 127C, 128N and 128C. The stimulated samples (10 min g1437) were labelled with TMT 129N, 129C, 130N, 130C and 131. After labelling, the TMT labelled samples were combined and lyophilized prior to phosphopeptide enrichment.

Human hepatocytes. Cell pellets (control or treated) were lysed in 20 µL of lysis buffer (6 M urea/2 M thiourea, 10 mM DTT, 1× PhosSTOP (Sigma) and 1 µL (4 µg) endoproteinase Lys-C (Vako Chemicals) and incubated at room temperature for 2 h. Then, iodoacetamide was added to the samples (20 mM final concentration) and incubated at room temperature for 30 min. These samples were then diluted 10× with 50 mM TEAB, pH 7.8 and sonicated using a Q125 probe sonicator (Qsonica sonicators; 2 × 10 s at 60% amplitude) on ice. After centrifugation at 14,000*g* for 20 min, the supernatant was collected and the protein concentration measured using Qubit fluorescence labelling (Thermo Fisher).

A total of 120 µg peptides was taken out for each sample and labelled with TMT 11 plex according to the manufacturer's protocol (Thermo Fisher). The TMT labelling was performed as follows: TMT 126 (Control), 127N (Control), 127C (Control), 128N (10 min g1437) and 128C (10 min g1437), 129N (10 min g1437), 129C (20 min g1437), 130N (20 min g1437) and 130C (20 min g1437). After labelling, the samples were combined and lyophilized prior to phosphopeptide enrichment.

Pooled liver samples. Pieces (3 mm^3) of liver from each individual mouse ($n = 3$) per treatment (vehicle or cotadutide) per time point (0, 2, 6 and 16 h) were pooled such that 8 samples were generated for testing (that is, vehicle or cotadutide for each timepoint). Each sample was homogenized in 1 mL ice-cold 0.1 M Na_2CO_3, pH 11 with protease (cOmplete Protease Inhibitor) and phosphatase inhibitors (PhosSTOP) + 10 mM sodium pervanadate using a Dounce homogenizer. After homogenization, the samples were sonicated using a Q125 probe sonicator (Qsonica) for 4 × 10 s on ice, with 20-s cooling intervals, with amplitude of 60%. The samples were ultracentrifuged at 100,000*g* for 90 min at 4 °C, and the supernatant stored at −20 °C pending analysis. The pellet was resuspended in 500 µL of 500 mM TEAB, pH 8. This solution was centrifuged at 14,000*g* for 30 min at 4 °C, the supernatant discarded and the pellet (membrane-enriched fraction) was re-dissolved in 6 M urea/2 M thiourea, 10 mM DTT and 1 µL (4 µg) endoproteinase Lys-C (Vako Chemicals) and incubated at room temperature for 2 h. The peptide cysteines were then alkylated using 20 mM iodoacetamide for 30 min in the dark. The solution was then diluted 10× with 20 mM TEAB, pH 7.8 and trypsin was added (5 µg) and incubated at room temperature overnight.

For the soluble proteins, these samples were treated as described for mouse hepatocyte soluble protein samples. A total of 120 µg peptides for soluble and membrane samples were labelled with TMT 10 plex (Thermo Fisher). For both fractions, the TMT labelling was performed as follows: vehicle 0 h (TMT126), vehicle 2 h (TMT127N), vehicle 6 h (TMT127C), vehicle 16 h (TMT128N), cotadutide 0 h (TMT128C), cotadutide 2 h (TMT129N), cotadutide 6 h (TMT129C) and cotadutide 16 h (TMT130N). After TMT labelling, the eight samples from soluble and membrane extractions were mixed, respectively, and lyophilized prior to PTM enrichment.

Enrichment of phosphopeptides. The purification of phosphorylated peptides was performed using titanium dioxide (TiO_2) chromatography, described in detail below[54]. To ensure high enrichment efficiency and to eliminate co-purified sialic acid containing *N*-linked glycopeptides, the phosphopeptides were purified using a double TiO_2 enrichment strategy with an enzymatic de-glycosylation step between the TiO_2 enrichment steps. The final phosphopeptide sample was fractionated using high-pH reversed-phase (HpH RP) separation prior to LC–MS/MS.

First TiO_2 enrichment step. The lyophilized TMT-labelled peptides were resuspended in TiO_2 loading buffer (80% acetonitrile (ACN), 5% trifluoracetic acid (TFA), 1 M glycolic acid) and incubated with 0.6 mg TiO_2 beads (GL Science) per 100 µg peptide on a shaker for 10 min. After incubation and centrifugation, the supernatant was incubated again with 3 mg TiO_2 beads on a shaker for 10 min. After incubation, all TiO_2 beads were sequentially washed together in 1 tube with 100 µL 80% ACN, 1% TFA and subsequently with 20% ACN, 0.1% TFA. All supernatants from the washes were collected, lyophilized and the 'non-modified' peptides were subsequently purified using HLB reversed-phase chromatography. The TiO_2 beads were dried and the bound peptides were eluted with 1% ammonium hydroxide solution, pH 11.3 on a shaker for 10 min. After incubation and centrifugation, the supernatant was lyophilized.

De-glycosylation. To remove the sialylated *N*-linked glycan structures from the enriched sialic acid containing *N*-linked glycopeptides that are co-enriched in the TiO_2, the dried peptides solution was resuspended in 100 µL 20 mM TEAB, pH 8,0 and treated with 2 µL *N*-glycosidase F (New England Biolabs) and 0.5 µL Sialidase A (Agilent) overnight at 37 °C.

Second TiO_2 enrichment step. The de-glycosylated sample was adjusted to 500 µL 70% ACN and 2% TFA and the TiO_2 beads used for the first TiO_2 enrichment were added to the solution and incubated on a shaker, as described above. After incubation, the beads were pelleted, and the supernatant was recovered. The TiO_2 beads were washed with 200 µL 50% ACN, 0.1% TFA, the beads were pelleted and the supernatant was recovered with the supernatant. The TiO_2 beads were dried and bound phosphopeptides were eluted from the beads with 1% ammonium hydroxide solution, pH 11.3 as described above. The phosphopeptides were lyophilized prior to HpH RP separation.

High-pH reversed-phase separation. The phosphorylated peptides were re-dissolved in 31 µL 20 mM ammonium formate, pH 9.3 and sonicated for 5 min. The sample with the phosphorylated peptides was then centrifuged for 15 min at 14,000*g* at room temperature and the supernatant was applied to an ACQUITY UPLC M-class CSH C18, 1.7 µm 300 µm × 100 mm RP column using a Dionex 3000 Ultimate system. The phosphopeptides were eluted from the C18 column with increasing concentrations of acetonitrile in ammonium formate (2, 50, 95% acetonitrile) for 155 min with a flow rate of 5.0 µL min^{-1}. The various phosphopeptide samples were fractionated into 15–20 concatenated fractions. The fractions were lyophilized prior to LC–MS/MS.

LC–MS/MS: phosphoproteomics. The various samples were analysed on an EASY nanoLC system coupled with a Fusion Lumos Tribrid orbitrap MS instrument or a Q-Exactive HF MS instrument. Lyophilized phosphopeptides from the HpH RP fractionation (15–20 concatenated fractions) were re-solubilized in 5 µL of 0.1% TFA and loaded onto a two-column system containing a 3-cm pre-column and a 17-cm analytical column, both consisting of fused silica capillary (75-µm inner diameter) packed with ReproSil – Pur C18 AQ 3 µm reversed-phase material. The peptides were eluted with an organic solvent gradient from 100% phase A (0.1% FA) to 40% phase B (95% ACN, 0.1% FA) at a constant flow rate of 300 nL min^{-1}. Depending on the sample, the gradient was either 60 min or 120 min for each fraction starting at 5% phase B up to 22% B for 50 or 90 min and then up to 40% phase B for 10 or 30 min. The EASY-nLC was online connected to a Fusion Lumos Tribrid orbitrap MS instrument or a Q-Exactive HF MS instrument (QE-HF MS (ThermoFisher)).

For the Lumos instrument, the automatic gain control target value of 1.5×10^6 ions and a maximum fill time of 50 ms was used. Each MS scan was acquired at high-resolution (120,000 full-width half-maximum (FWHM)) at 200 *m/z* in the Orbitrap with a mass range of 400–1,400 Da. The instrument was set to select as many precursor ions as possible in 3 s between the MS analyses. Phosphopeptide ions were selected from the MS for higher energy collision-induced dissociation (HCD) fragmentation (collision energy, 40%). Fragmentation was detected in the orbitrap at high resolution (60,000 FWHM) for a target value of 1×10^5 ions and a maximum injection time of 150 ms using an isolation window of 0.7 Da and a dynamic exclusion of 30 s.

For the QE-HF MS, a full MS scan with an AGC target value of 3×10^6 ions and a maximum fill time of 100 ms was used. Each MS scan was acquired at high resolution (120,000 FWHM) at 200 *m/z* in the Orbitrap with a mass range of 400–1,600 Da. The 15 most abundant peptide ions were selected from the MS for HCD fragmentation (collision energy: 31V). Fragmentation was performed at high resolution (60,000 FWHM) for a target of 1×10^5 and a maximum injection time of 150 ms using an isolation window of 1.2 Da and a dynamic exclusion of 10 s. All raw data were viewed in Xcalibur v3.0 (Thermo Fisher).

Phosphopeptide identification and quantitation. All LC–MS/MS raw data files were searched using Proteome Discoverer (PD) version 2.2. The raw data were searched in PD using a workflow where the raw data were first subjected to database searching using an in-house Mascot server (Version 2.2.04, Matrix Science). The searches had the following criteria: database, SwissProt human protein database (version 17.07.2017; 75193 sequences); enzyme, trypsin; maximum missed cleavages, 2; fixed modifications, TMT6plex (amino-terminal), TMT6plex (K) and carbamidomethyl (C). Variable modification for the phosphopeptides was phospho (S/T/Y) and deamidation (N). Peptides were accepted for further analysis if they had a *q* value below 0.01 (Percolator)[55,56], corresponding to 1% false-discovery rate, had Mascot rank 1 and a cut-off value of Mascot score >18 (ref. [57]).

The TMT10 plex reporter ion signals were quantified using S/N and they were normalized to the total peptide S/N in the PD program. The in-built ANOVA test in PD was used to generate *P* values for all the phosphopeptides analysed here. With low number of replicates (for example, pooled liver samples) a *t*-test was performed so that the ratio of a protein or peptide is compared to 200 protein/peptide ratios with approximately the same intensity, providing more reliable *P* values for a low number of replicates[58].

Metabolomics and lipidomics. Samples were prepared and analysed for global metabolomic and lipidomic profiling at Metabolon[59,60]. For global metabolomics, liver samples were homogenized in water prior to extraction at a constant volume per mass. Liver homogenate and serum samples were extracted with methanol in the presence of recovery standards under vigorous shaking followed by centrifugation. The extracts were aliquoted, dried under nitrogen and reconstituted in appropriate solvents containing internal standards. The aliquots were analysed by ultra-performance LC–MS/MS using four different methods: two with acidic positive-ion conditions, one with basic negative-ion conditions and one with negative ionization which was optimized for polar compounds. Metabolites were identified by comparison of chromatographic and MS data to a reference library of chemical standards. For lipidomic profiling, samples were extracted in the presence of deuterated internal standards. Serum samples were prepared using an automated butanol:methanol extraction procedure incorporating heptane:ethylacetate and acetic acid phase separation based on a previously described method[61]. Liver samples were soaked overnight at 4 °C in dichloromethane:methanol (50:50) at a constant volume per mass, and then lipids were extracted from the supernatant using a modified Bligh-Dyer extraction. Extracts were dried under nitrogen and reconstituted in dichloromethane:methanol (50:50) containing 10 mM ammonium acetate. Lipids were analysed on a Sciex SelexIon-5500 QTRAP operated in multiple-reaction monitoring mode with both positive- and negative-mode electrospray. Individual lipid species were quantified on the basis of the concentration of assigned internal standards added to the samples and the ratio of the signal intensity of each target compound to that of its assigned internal standard. Lipid class concentrations were calculated from the sum of all molecular species within a class. Fatty acid compositions were determined on the basis of the proportion of individual fatty acids in each lipid class.

Statistics. All statistical analyses were carried out using GraphPad Prism 7 (GraphPad Software). The data were analysed via Student's *t*-test or one-way or two-way ANOVA as indicated in each figure, with post hoc tests as indicated in the figure legends. Values of $P \leq 0.05$ were considered to represent statistically significant differences.

Reporting Summary. Further information on research design is available in the Nature Research Reporting Summary linked to this article.

Data availability

The datasets generated during these studies are available from the corresponding author on reasonable request. These datasets include: in vivo data for the mouse studies and encompass metabolic, biochemical and histological data/images; mass spectrometry data from mouse liver and/or serum, mouse hepatocytes or human hepatocytes; imaging and quantitation data for mitochondrial analyses; qRT–PCR data for select gene expression analyses. RNA-seq datasets are available in the SRA database with accession number PRJNA574649.

Received: 28 August 2018; Accepted: 20 April 2020;
Published online: 21 May 2020

References

1. Younossi, Z. et al. Global burden of NAFLD and NASH: trends, predictions, risk factors and prevention. *Nat. Rev. Gastroenterol. Hepatol.* **15**, 11–20 (2018).
2. Ibrahim, S. H., Hirsova, P. & Gores, G. J. Non-alcoholic steatohepatitis pathogenesis: sublethal hepatocyte injury as a driver of liver inflammation. *Gut* **67**, 963–972 (2018).
3. Friedman, S. L., Neuschwander-Tetri, B. A., Rinella, M. & Sanyal, A. J. Mechanisms of NAFLD development and therapeutic strategies. *Nat. Med.* **24**, 908–922 (2018).
4. Cusi, K. Treatment of patients with type 2 diabetes and non-alcoholic fatty liver disease: current approaches and future directions. *Diabetologia* **59**, 1112–1120 (2016).
5. Bueter, M. & le Roux, C. W. Gastrointestinal hormones, energy balance and bariatric surgery. *Int. J. Obes.* **35**(Suppl. 3), S35–S393 (2011).
6. Ionut, V., Burch, M., Youdim, A. & Bergman, R. N. Gastrointestinal hormones and bariatric surgery-induced weight loss. *Obesity* **21**, 1093–1103 (2013).
7. Meek, C. L., Lewis, H. B., Reimann, F., Gribble, F. M. & Park, A. J. The effect of bariatric surgery on gastrointestinal and pancreatic peptide hormones. *Peptides* **77**, 28–37 (2016).
8. Cohen, M. A. et al. Oxyntomodulin suppresses appetite and reduces food intake in humans. *J. Clin. Endocrinol. Metab.* **88**, 4696–4701 (2003).
9. Wynne, K. et al. Oxyntomodulin increases energy expenditure in addition to decreasing energy intake in overweight and obese humans: a randomised controlled trial. *Int. J. Obes.* **30**, 1729–1736 (2006).
10. Scott, R., Minnion, J., Tan, T. & Bloom, S. R. Oxyntomodulin analogue increases energy expenditure via the Gcg receptor. *Peptides* **104**, 70–77 (2018).
11. Ambery, P. et al. Cotadutide, a GLP-1 and Gcg receptor dual agonist, in obese or overweight patients with type 2 diabetes: a randomised, controlled, double-blind, ascending dose and phase 2a study. *Lancet* **10140**, 2607–2618 (2018).
12. Day, J. W. et al. A new Gcg and GLP-1 co-agonist eliminates obesity in rodents. *Nat. Chem. Biol.* **5**, 749–757 (2009).
13. Henderson, S. J. et al. Robust anti-obesity and metabolic effects of a dual GLP-1/Gcg receptor peptide agonist in rodents and non-human primates. *Diabetes Obes. Metab.* **18**, 1176–1190 (2016).
14. Khajavi, N., Biebermann, H., Tschop, M. & DiMarchi, R. Treatment of diabetes and obesity by rationally designed peptide agonists functioning at multiple metabolic receptors. *Endocr. Dev.* **32**, 165–182 (2017).
15. Tan, T. M. et al. Coadministration of Gcg-like peptide-1 during Gcg infusion in humans results in increased energy expenditure and amelioration of hyperglycemia. *Diabetes* **62**, 1131–1138 (2013).
16. Pocai, A. et al. Glucagon-like peptide 1/Gcg receptor dual agonism reverses obesity in mice. *Diabetes* **58**, 2258–2266 (2009).
17. Patel, V. et al. Coagonist of GLP-1 and Gcg receptor ameliorates development of non-alcoholic fatty liver disease. *Cardiovasc. Hematol. Agents Med. Chem.* **16**, 35–43 (2018).
18. Patel, V. et al. Coagonist of Gcg-like peptide-1 and Gcg receptors ameliorates nonalcoholic fatty liver disease. *Can. J. Physiol. Pharmacol.* **96**, 587–596 (2018).
19. Valdecantos, M. P. et al. A novel Gcg-like peptide 1/Gcg receptor dual agonist improves steatohepatitis and liver regeneration in mice. *Hepatology* **65**, 950–968 (2017).
20. Hansen, H. H. et al. Mouse models of nonalcoholic steatohepatitis in preclinical drug development. *Drug Discov. Today* **22**, 1707–1718 (2017).
21. Koliaki, C. et al. Adaptation of hepatic mitochondrial function in humans with non-alcoholic fatty liver is lost in steatohepatitis. *Cell Metab.* **21**, 739–746 (2015).
22. Boland, M. L. et al. Nonalcoholic steatohepatitis severity is defined by a failure in compensatory antioxidant capacity in the setting of mitochondrial dysfunction. *World J. Gastroenterol.* **24**, 1748–1765 (2018).
23. Shaw, R. J. et al. The kinase LKB1 mediates glucose homeostasis in liver and therapeutic effects of metformin. *Science* **310**, 1642–1646 (2005).
24. Lawitz, E. J. et al. Acetyl-CoA carboxylase inhibitor GS-0976 for 12 weeks reduces hepatic de novo lipogenesis and steatosis in patients with nonalcoholic steatohepatitis. *Clin. Gastroenterol. Hepatol.* **16**, 1983–1991 (2018).
25. Koo, S.-H. et al. The CREB coactivator TORC2 is a key regulator of fasting glucose metabolism. *Nature* **437**, 1109–1113 (2005).
26. Dulai, P. S. et al. Increased risk of mortality by fibrosis stage in nonalcoholic fatty liver disease: systematic review and meta-analysis. *Hepatology* **65**, 1557–1565 (2017).
27. Armstrong, M. J. et al. Liraglutide safety and efficacy in patients with non-alcoholic steatohepatitis (LEAN): a multicentre, double-blind, randomised, placebo-controlled phase 2 study. *Lancet* **387**, 679–690 (2016).
28. Loomba, R. et al. GS-0976 reduces hepatic steatosis and fibrosis markers in patients with nonalcoholic fatty liver disease. *Gastroenterology* **155**, 1463–1473 (2018).
29. Neuschwander-Tetri, B. A. et al. Farnesoid X nuclear receptor ligand obeticholic acid for non-cirrhotic, non-alcoholic steatohepatitis (FLINT): a multicentre, randomised, placebo-controlled trial. *Lancet* **385**, 956–965 (2015).
30. Ayala, J. E. et al. Hyperinsulinemic–euglycemic clamps in conscious, unrestrained mice. *J. Vis. Exp.* e3188 (2011).
31. Steele, R., Wall, J. S., De Bodo, R. C. & Altszuler, N. Measurement of size and turnover rate of body glucose pool by the isotope dilution method. *Am. J. Physiol.* **187**, 15–24 (1956).

32. Bederman, I. R., Foy, S., Chandramouli, V., Alexander, J. C. & Previs, S. F. Triglyceride synthesis in epididymal adipose tissue: contribution of glucose and non-glucose carbon sources. *J. Biol. Chem.* **284**, 6101–6108 (2009).
33. Hasenour, C. M. et al. Mass spectrometry-based microassay of ^{2}H and ^{13}C plasma glucose labeling to quantify liver metabolic fluxes in vivo. *Am. J. Physiol. Endocrinol. Metab.* **309**, E191–E203 (2015).
34. Young, J. D. INCA: a computational platform for isotopically non-stationary metabolic flux analysis. *Bioinformatics* **30**, 1333–1335 (2014).
35. Hughey, C. C. et al. Loss of hepatic AMP-activated protein kinase impedes the rate of glycogenolysis but not gluconeogenic fluxes in exercising mice. *J. Biol. Chem.* **292**, 20125–20140 (2017).
36. Chan, T. M. & Exton, J. H. A method for the determination of glycogen content and radioactivity in small quantities of tissues or isolated hepatocytes. *Anal. Biochem.* **71**, 96–105 (1976).
37. Yang, D. et al. Assay of low deuterium enrichment of water by isotopic exchange with [U-13C3]acetone and gas chromatography-mass spectrometry. *Anal. Biochem.* **258**, 315–321 (1998).
38. Previs, S. F. et al. Using [^{2}H]water to quantify the contribution of de novo palmitate synthesis in plasma: enabling back-to-back studies. *Am. J. Physiol. Endocrinol. Metab.* **315**, E63–e71 (2018).
39. Burgess, S. C. et al. Impaired tricarboxylic acid cycle activity in mouse livers lacking cytosolic phosphoenolpyruvate carboxykinase. *J. Biol. Chem.* **279**, 48941–48949 (2004).
40. Antoniewicz, M. R., Kelleher, J. K. & Stephanopoulos, G. Measuring deuterium enrichment of glucose hydrogen atoms by gas chromatography/mass spectrometry. *Anal. Chem.* **83**, 3211–3216 (2011).
41. Kristiansen, M. N. et al. Obese diet-induced mouse models of nonalcoholic steatohepatitis-tracking disease by liver biopsy. *World J. Hepatol.* **8**, 673–684 (2016).
42. Barascuk, N. et al. A novel assay for extracellular matrix remodeling associated with liver fibrosis: an enzyme-linked immunosorbent assay (ELISA) for a MMP-9 proteolytically revealed neo-epitope of type III collagen. *Clin. Biochem.* **43**, 899–904 (2010).
43. Leeming, D. J. et al. Enzyme-linked immunosorbent serum assay specific for the 7S domain of Collagen Type IV (P4NP 7S): a marker related to the extracellular matrix remodeling during liver fibrogenesis. *Hepatol. Res.* **42**, 482–493 (2012).
44. Vassiliadis, E. et al. Immunological detection of the type V collagen propeptide fragment, PVCP-1230, in connective tissue remodeling associated with liver fibrosis. *Biomarkers* **16**, 426–433 (2011).
45. Ouberai, M. M. et al. Controlling the bioactivity of a peptide hormone in vivo by reversible self-assembly. *Nat. Commun.* **8**, 1026 (2017).
46. Kleiner, D. E. et al. Design and validation of a histological scoring system for nonalcoholic fatty liver disease. *Hepatology* **41**, 1313–1321 (2005).
47. Glick, D. et al. BNip3 regulates mitochondrial function and lipid metabolism in the liver. *Mol. Cell Biol.* **32**, 2570–2584 (2012).
48. Michopoulos, F. et al. Targeted profiling of polar intracellular metabolites using ion-pair-high performance liquid chromatography and -ultra high performance liquid chromatography coupled to tandem mass spectrometry: applications to serum, urine and tissue extracts. *J. Chromatogr. A.* **1349**, 60–68 (2014).
49. Dobin, A. et al. STAR: ultrafast universal RNA-seq aligner. *Bioinformatics* **29**, 15–21 (2013).
50. Subramanian, A. et al. Gene set enrichment analysis: a knowledge-based approach for interpreting genome-wide expression profiles. *Proc. Natl Acad. Sci. USA* **102**, 15545–15550 (2005).
51. Liberzon, A. et al. Molecular signatures database (MSigDB) 3.0. *Bioinformatics* **27**, 1739–1740 (2011).
52. Liberzon, A. et al. The Molecular Signatures Database (MSigDB) hallmark gene set collection. *Cell Syst.* **1**, 417–425 (2015).
53. Hanzelmann, S., Castelo, R. & Guinney, J. GSVA: gene set variation analysis for microarray and RNA-seq data. *BMC Bioinformatics* **14**, 7 (2013).
54. Kang, T. et al. Characterization of the molecular mechanisms underlying glucose stimulated insulin secretion from isolated pancreatic beta-cells using post-translational modification specific proteomics (PTMomics). *Mol. Cell Proteomics* **17**, 95–110 (2018).
55. The, N. et al. Fast and accurate proteim false discovery rates on large-scale proteomics data sets with percolator 3.0. *J. Am. Soc. Mass Spectrom.* **27**, 1719–1727 (2016).
56. Käll, L. et al. Semi-supervised learning for peptide identification from shotgun proteomics datasets. *Nat. Methods* **4**, 923–925 (2007).
57. Marx, H. et al. A large synthetic peptide and phosphopeptide reference library for mass spectrometry-based proteomics. *Nat. Biotechnol.* **13**, 557–566 (2013).
58. Navarro, P. et al. General statistical framework for quantitative proteomics by stabe isotope labeling. *J. Proteome Res.* **13**, 1234–1247 (2014).
59. Zierer, J. et al. The fecal metabolome as a functional readout of the gut microbiome. *Nat. Genet.* **50**, 790–795 (2018).
60. Zhang, M. et al. Adipocyte-derived lipids mediate melanoma progression via FATP proteins. *Cancer Discov.* **8**, 1006–1025 (2018).
61. Lofgren, L. et al. The BUME method: a novel automated chloroform-free 96-well total lipid extraction method for blood plasma. *J. Lipid. Res.* **53**, 1690–1700 (2012).

Acknowledgements

The authors wish to thank the Lab Animal Resource staff at MedImmune/AstraZeneca for their assistance with animal husbandry and care. We thank D. Leeming and M. Karsdal (Nordic Biosciences, Denmark) for assistance with circulating collagen fragment detection and interpretation. We thank K. Hightower (Metabolon, Durham, NC) for assistance with metabolomics analyses and interpretation. The authors also wish to thank M. Jain (AstraZeneca, Cambridge, UK) for critical review and comments on the manuscript during preparation. The Villum Center for Bioanalytical Sciences at University of Southern Denmark is acknowledged for access to high-end MS instruments. Vanderbilt MMPC and their NIH funding (DK059637).

Author contributions

M.L.B., R.C.L., A.N., M.F., M.R.L., L.L., O.P.M. and J.L.T. designed experiments; M.L.B., R.C.L., A.N., S.O., B.B.B., H.L., J.C., K.M., J.N., M.F., M.R.L., L.L., O.P.M., C.J.R. and J.L.T. collected and/or analysed and interpreted experimental data; S.G. and S.S.V. provided pathology analysis of mouse NASH studies; M.L.B, R.C.L., J.G., M.R.L, C.J.R. and J.L.T. wrote the paper; C.M.R. and L.J. reviewed and edited the manuscript.

Competing interests

The authors declare competing interests as defined by Nature Research. Employee of AstraZeneca (R.C.L., K.M., S.O., J.C., J.N., J.G., L.J., C.J.R.). Owns stock in AstraZeneca (K.M., S.O., J.C., J.N., J.G., L.J., C.M.R., J.L.T., C.J.R.).

Additional information

Extended data is available for this paper at https://doi.org/10.1038/s42255-020-0209-6.

Supplementary information is available for this paper at https://doi.org/10.1038/s42255-020-0209-6.

Correspondence and requests for materials should be addressed to C.J.R.

Reprints and permissions information is available at www.nature.com/reprints.

Publisher's note Springer Nature remains neutral with regard to jurisdictional claims in published maps and institutional affiliations.

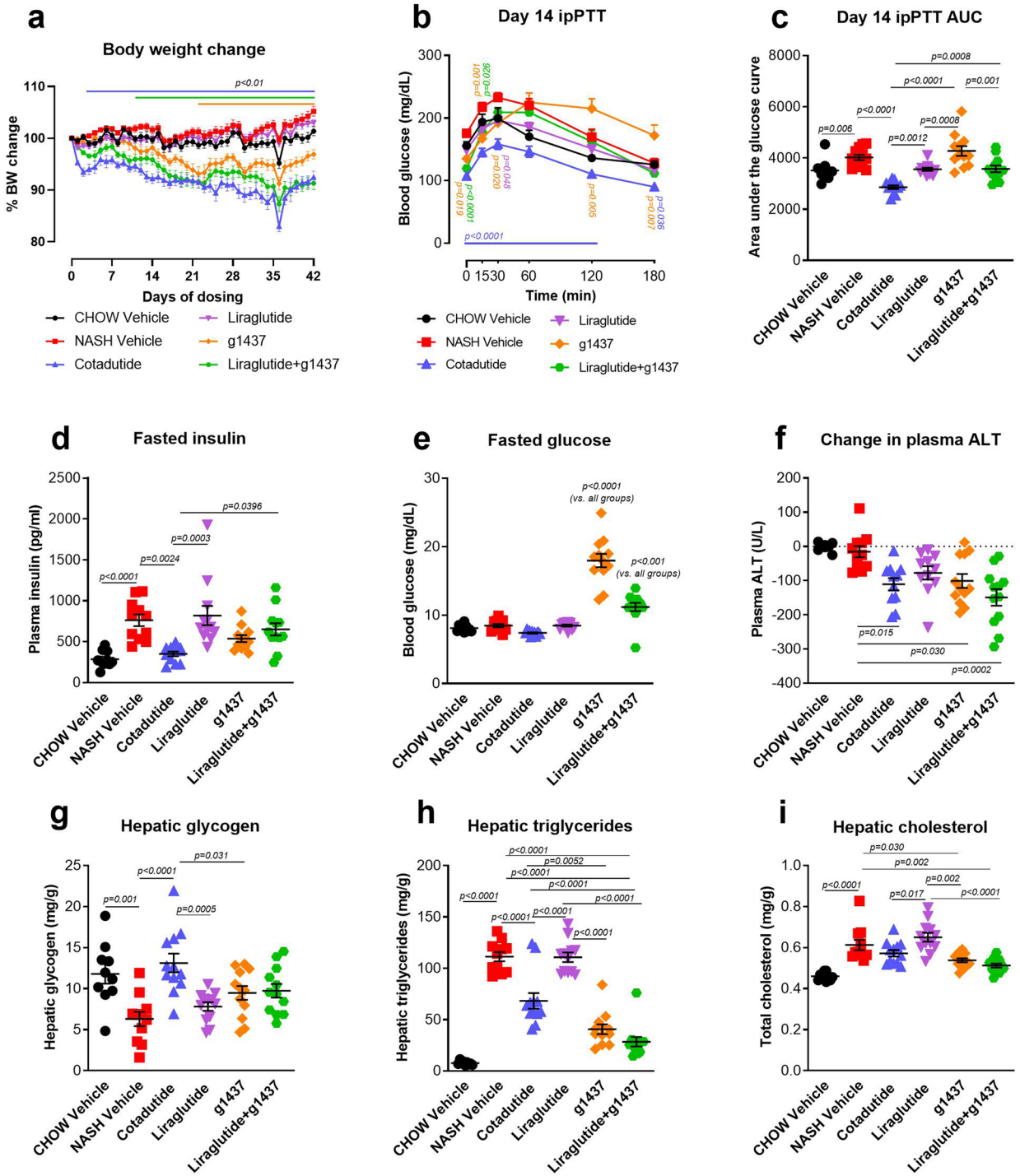

Extended Data Fig. 1 | Metabolic and hepatic parameters following six-week treatment of NASH C57Bl6/J mice. Mice were treated with cotadutide, liraglutide, g1437 or liraglutide+g1437 at equimolar dosing (10 nmol/kg, SC, QD for 42 days) compared to vehicle. Animals were given *ad libitum* access to food for the entirety of the study except on day 14 mice were fasted for 6 h prior to ipPTT. **a**, Reduction in body weight throughout the 42-day dosing period shown as % change. **b**, Blood glucose profile during ipPTT (pyruvate given at dose of 2g/kg) and (**c**) area under the ipPTT curve. **d**, Fasting plasma insulin, (**e**) fasting blood glucose and (**f**) plasma ALT levels at the end of the study. **g**, Terminal liver glycogen content, (**h**) triglycerides and (**i**) cholesterol. Chow vehicle (n=10); NASH vehicle (n=11); Cotadutide (n=12); Liraglutide (n=12); g1437 (n=12); Liraglutide+g1437 (n=12). Data shown as the mean ± SEM. (**a** and **b**) Two-way ANOVA, Tukey's multiple comparisons post-hoc test. In (**a** and **b**) colored lines and p-values indicated differences for the corresponding treatment group compared with NASH vehicle at each time point. **c-i**, Two-sided student's t-test for chow controls vs. NASH vehicle to determine effect of NASH diet; One-way ANOVA, Tukey's multiple comparisons post-hoc test, chow group excluded.

Uniprot	Protein, Gene	Phosphosite (previously identified PKA substrate in bold)	PKA consensus	Human site	Identified in Primary Human Hepatocytes	Function	Previously Identified Phosphosite	Supplementary Reference #
Q61606	glucagon receptor, *Gcgr*	S432/S433/S436	yes (S432)	S431	no	Glucagon receptor	yes	4
P05132	PKA catalytic subunit a, *Prkaca*	S339	yes	S339	yes	Kinase	yes	4,5
P35569	insulin receptor substrate 1, *Irs1*	S325	yes	S330	no	insulin receptor second messenger	yes	6
P81122	insulin receptor substrate 2, *Irs2*	S556	yes	S560	no	insulin receptor second messenger	yes (Plk1)	7
Q5EG47	AMPK catalytic subunit alpha-1, *Prkaa1*	T490	no	T490	yes	Kinase	yes	4
		S496	yes	S496	no		yes	8
Q8BRK8	AMPK catalytic subunit alpha-2, *Prkaa2*	S481	no	S481	no	Kinase	yes	5
Q9R078	AMPK non-catalytic subunit beta-1, *Prkab1*	**S24**	yes	S24	yes	Kinase	yes	9
Q6PAM0	AMPK non-catalytic subunit beta-2, *Prkab2*	S38	no	S39	no	Kinase	yes	4,10
Q91WG5	AMPK non-catalytic subunit gamma-2, *Prkag2*	S131/S135	yes (both)	S131/S135	no/no	Kinase	yes	4,11
P12382	ATP-dependent 6-phosphofructokinase, liver type , *Pfkl*	S775	yes	S775	no	converts fructose-6-phosphate to fructose-1,6-bisphosphate	yes	4
A7UAK5	6-phosphofructo-2-kinase/fructose-2, 6-biphosphatase 3 splice variant 2, *Pfkfb3*	S490	yes	S461	yes	converts fructose-6-phosphate to fructose-2,6-bisphosphate	yes	12
Q2NL51	Glycogen synthase kinase-3 alpha, *Gsk3a*	**S21**	yes	S21	yes	pleiotropic kinase; phosphorylates and inhibits glycogen synthase	yes	13
Q9Z1E4	glycogen synthase 1, *Gys1*	S698/S702	yes (698)	S698/S702	yes/no	responsible for the conversion of glucose into glycogen	yes	14
		S711	yes	S710	no		yes	14
Q8BWJ3	Phosphorylase b kinase regulatory subunit alpha, liver isoform, *Phka2*	S637, S640	yes (637)	S637/S640	no/no	phosphorylates and activates glycogen phosphorylase	no	
		S729	yes	S729	yes		yes	5
Q7TSH2	Phosphorylase b kinase regulatory subunit beta , *Phkb*	**S19**	yes	S27	yes	phosphorylates and activates glycogen phosphorylase	yes	15
Q9ET01	Glycogen phosphorylase, liver form, *Pygl*	T214	no	T214	no	catalyzes the release of glucose-1-phosphate from glycogen	no	
		S430	yes	S430	yes		yes	16
		T520	no	T520	no		no	
Q91ZJ5	UTP--glucose-1-phosphate uridylyltransferase , *Ugp2*	S13	yes	S13	no	converts UTP and glucose-1-phosphate to diphosphate and UDP-glucose	yes	5
Q99MZ3	Carbohydrate-responsive element-binding protein, *Mlxipl*	S195	no	S195	no	promotes the transcription of lipid synthesis genes	no	
		S196	yes	S196	no		yes	11,17
		S366	yes	S361	no		yes	17
Q3V117	ATP-citrate synthase, *Acly*	S455	yes	S455	yes	catalyzes the conversion of citrate to acetyl-CoA	yes (Akt)	18
E9Q4Z2	Acetyl-CoA carboxylase 2, *Acacb*	S81	yes	S91	no	catalyzes rate limiting step of FA biosynthesis	yes	17
Q61586	Glycerol-3-phosphate acyltransferase 1, mitochondrial, *Gpam*	S694	no	S695	no	catalyzes the initial step of glycerolipid synthesis	yes	14
Q9Z2A7	Diacylglycerol O-acyltransferase 1, *Dgat1*	T15/S20	yes, yes	T12/S17	yes/yes	catalyzes formation of triglycerides from diacylglycerol and acyl-CoA	yes	19
		S17/S20	yes, yes	S14/S17	yes/yes		yes	19
		S20	yes	S17	yes		yes	19
P54310	Hormone-sensitive lipase , *Lipe*	**S557**	yes	S552	no	catalyzes the release of FFA from triglycerides and DAGs	yes	20
P16220	Cyclic AMP-responsive element-binding protein 1, *Creb1*	S142	no	S142	yes	transcription factor that responds to cAMP	yes	21

Extended Data Fig. 2 | Table of phosphopeptides. Description of hepatic phosphopeptides detected in primary mouse and human hepatocytes following treatment with g1437.

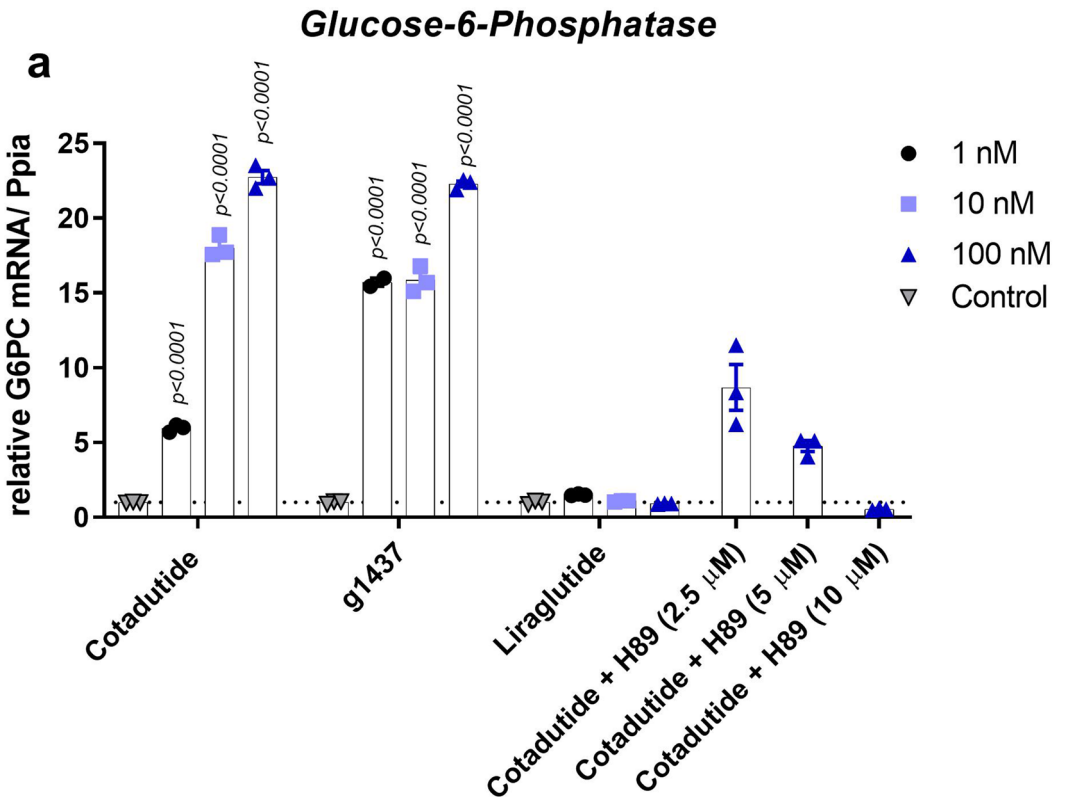

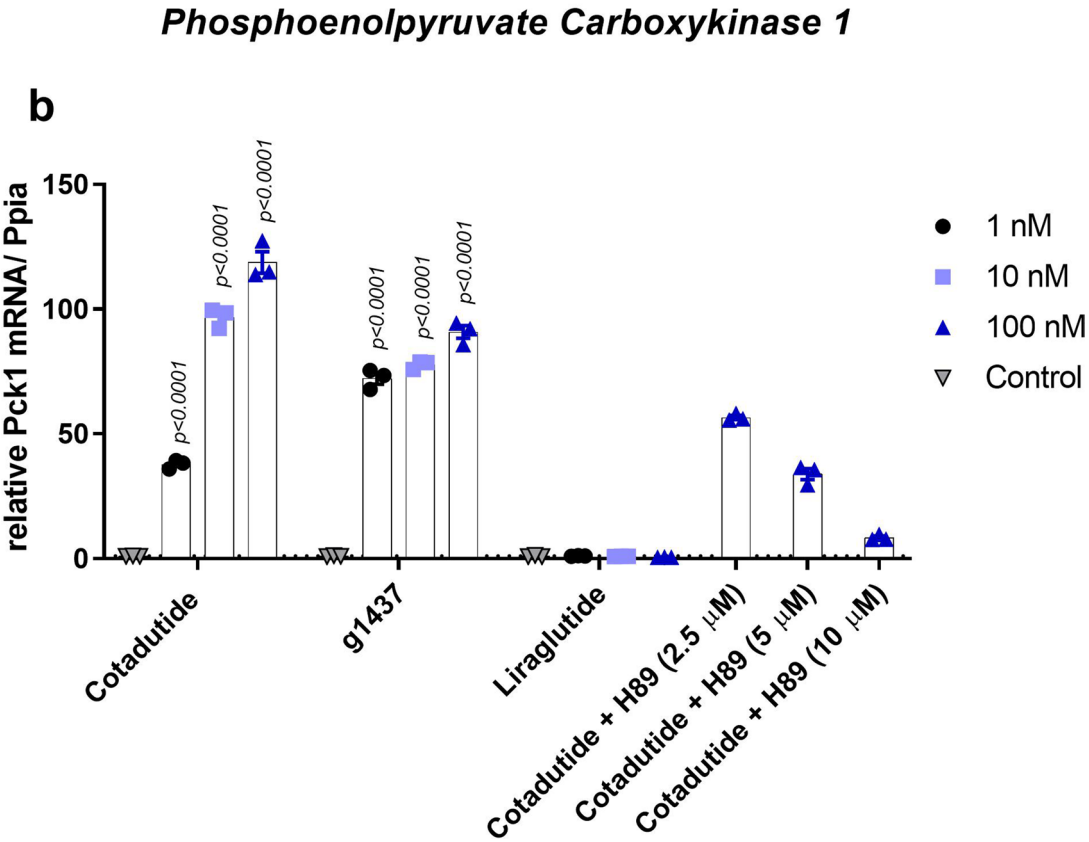

Extended Data Fig. 3 | Table of phosphopeptides. Description of hepatic phosphopeptides detected in primary mouse and human hepatocytes following treatment with g1437.

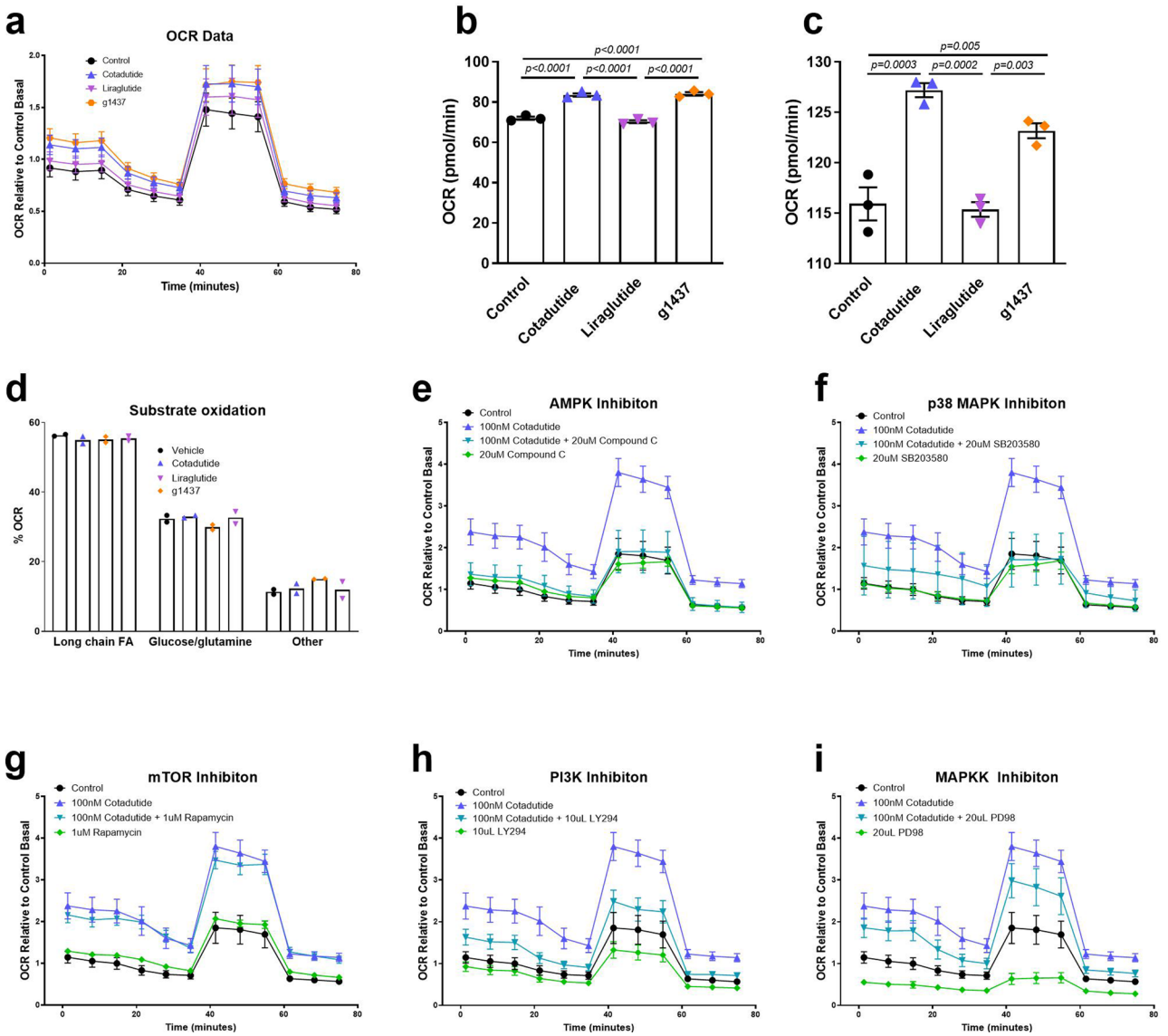

Extended Data Fig. 4 | Cotadutide improves mitochondrial respiratory function in primary mouse hepatocytes through Gcg signaling mechanisms. **a**, Mitochondrial oxygen consumption rate (OCR) during mitochondrial stress test of healthy primary murine hepatocytes treated *ex vivo* for 4h with 100 nM cotadutide, g1437 or liraglutide compared to vehicle control hepatocytes (n=3 biologically independent samples/group). **b**, Basal respiration and (**c**) maximal respiration measured following injection of uncoupler FCCP. **d**, Oxygen consumption of primary mouse hepatocytes shown as the percentage of total respiration that is driven by the oxidation of indicated substrates (n=2 biologically independent samples/group). **e**-**i**, Oxygen consumption of mouse primary hepatocytes, during mitochondrial stress test, treated with cotadutide +/- Ampk inhibitor, Compound C (**e**; 20 uM), p38Mapk inhibitor, SB203580 (**f**; 20 um), mTor inhibitor, Rapamycin (**g**; 1 uM), Pi3 inhibitor, LY294 (**h**; 10 uM) or Mapkk inhibitor, PD98 (**i**; 20 uM) compared with control treated hepatocytes. n=6 replicates from 1 biological samples for all except for Cotadutide; Cotadutide+SB203580; Rapamycin; Cotadutide+Rapamycin; PD98; Cotadutide+PD98 in which 5 replicates were performed. The experiment was performed on 3 separate occasions with similar results. All data shown as the mean ± SEM. **b-d**, One-way ANOVA with Dunnett's multiple comparisons post-hoc test.

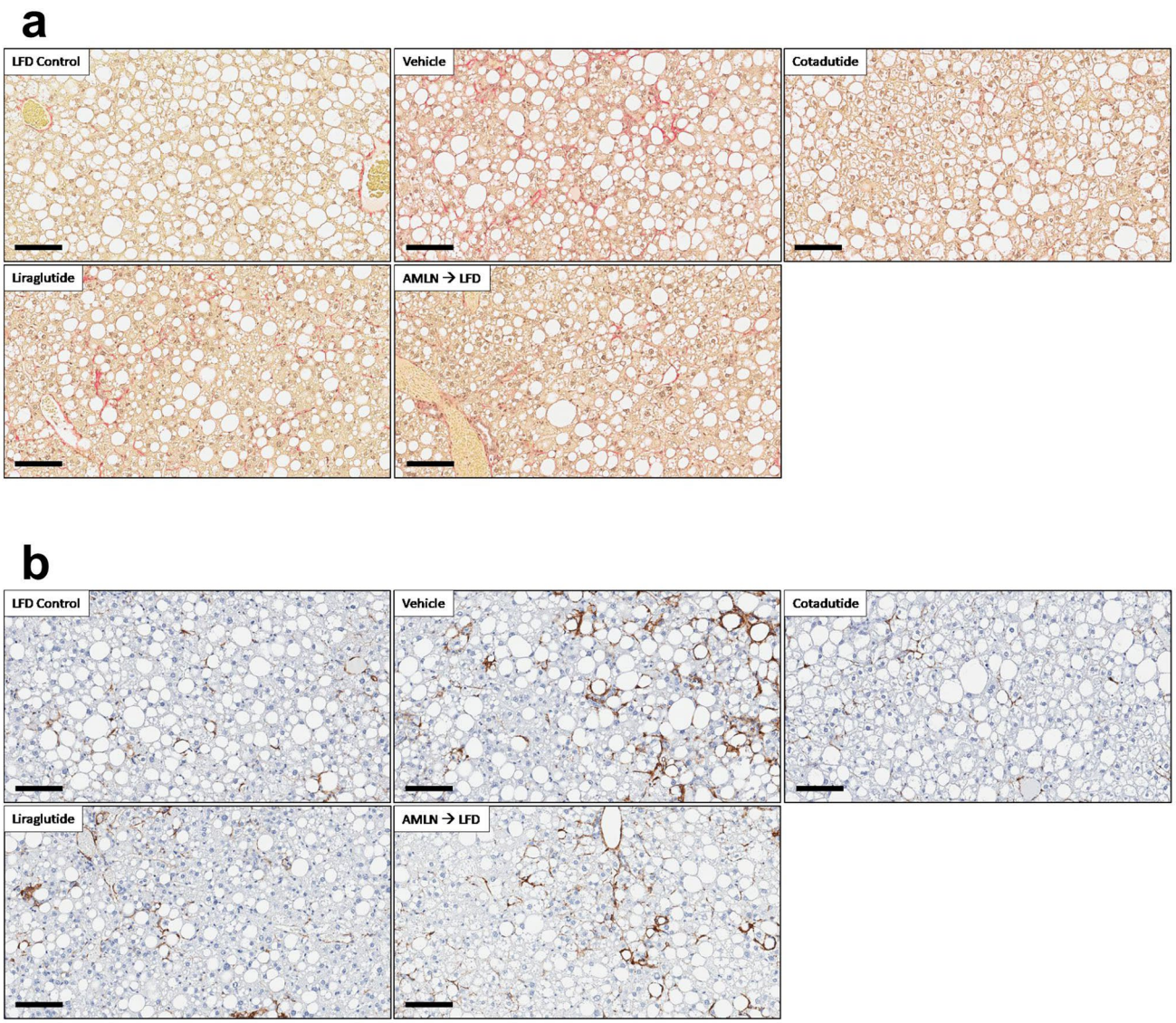

Extended Data Fig. 5 | Cotadutide reduces hepatic fibrosis and inflammation corresponding to animals shown in Figs. 7 and 8. a, representative αSma stained liver sections, quantification is provided in Fig. 8d. Scale bar = 100 μm. **b**, representative PSR stained liver sections, quantification is provided in Fig. 8e. Scale bar = 100 μm. These experiments were performed in ob/ob mice with LFD (n=8); AMLN vehicle (n=11); Cotadutide (n=7); Liraglutide (n= 10); AMLN-to-LFD (n=10) mice/group.

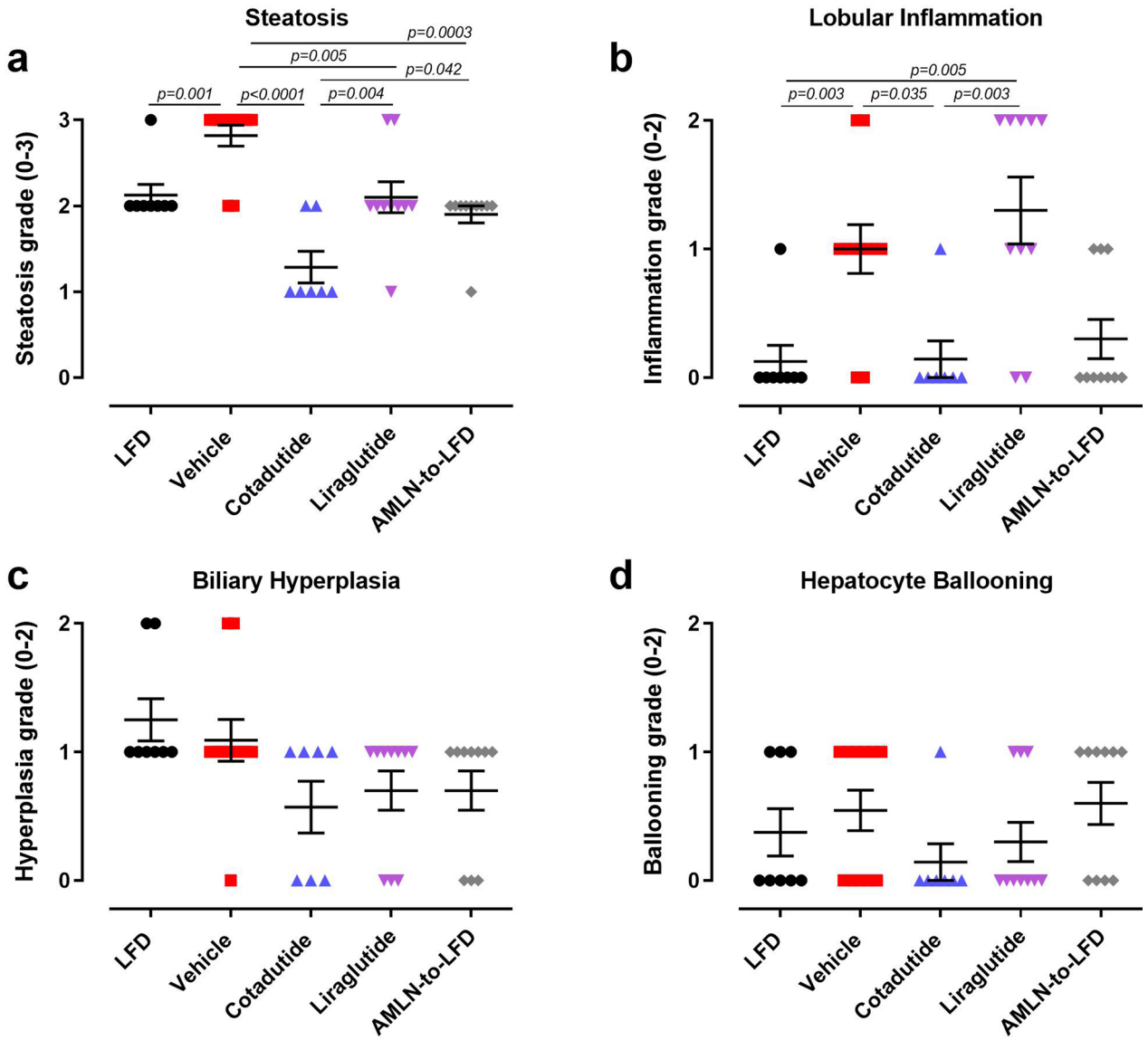

Extended Data Fig. 6 | Grades of histopathological NASH features corresponding to animals in Figs. 7 and 8. a, steatosis grade, (**b**) lobular inflammation, (**c**) biliary hyperplasia and (**d**) hepatocyte ballooning. LFD (n=8); Vehicle (n=11); Cotadutide (n=7); Liraglutide (n=10); AMLN-to-LFD (n=10). Data represented as the mean ± SEM. Two-sided student's t-test for LFD vs. vehicle to determine effect of NASH diet; one-way ANOVA, Tukey's multiple comparison post-hoc test, LFD group excluded.

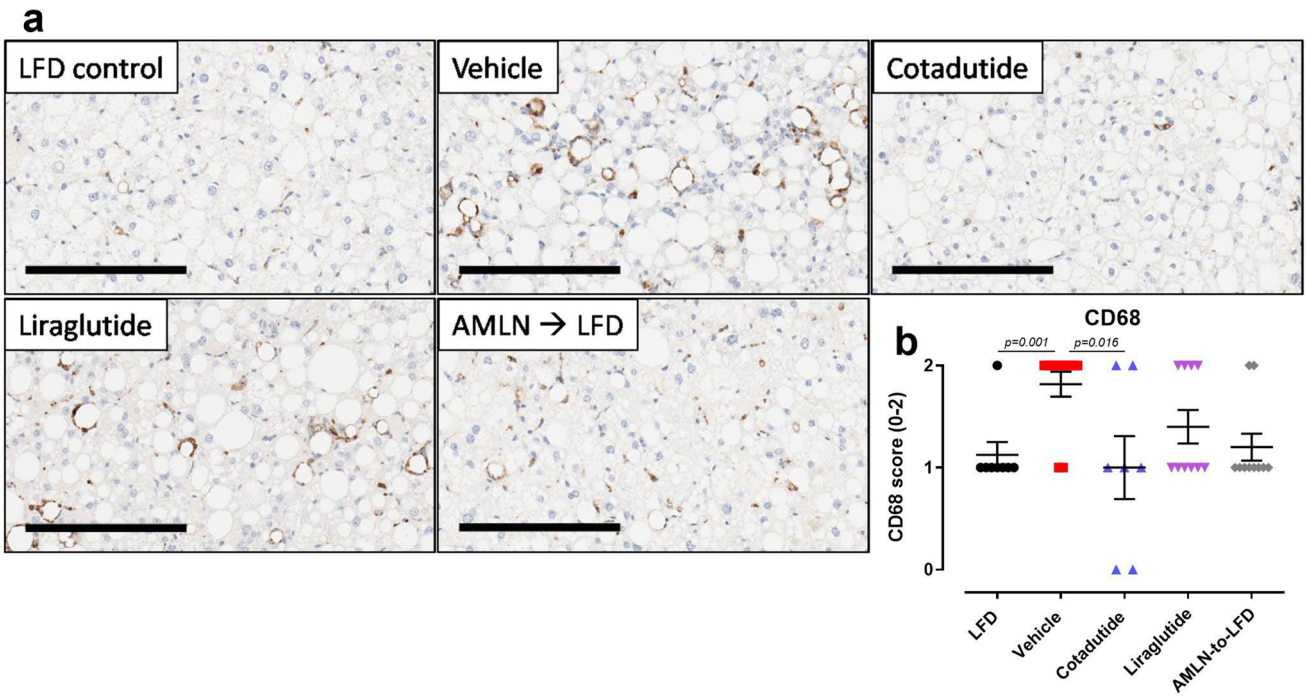

Extended Data Fig. 7 | CD68, a marker of immune cell infiltration, is reduced by Cotadutide in animals corresponding to Figs. 7 and 8. a, Representative images of CD68 IHC staining of mouse liver and the (**b**) pathologist graded scoring. LFD control slides are set to baseline of 1 to account for resident Kupffer cells (dark stained spots disperse equally between hepatocytes). Infiltration of immune cells identified by accumulation around vacuoles we scored relative to the baseline. Scale bar = 200 μm. LFD (n=8); Vehicle (n=11); Cotadutide (n=7); Liraglutide (n=10); AMLN-to-LFD (n=10). Data represented as the mean ± SEM. Two-sided student's t-test for LFD vs. vehicle to determine effect of NASH diet; One-way ANOVA, Tukey's multiple comparisons post-hoc test, LFD group excluded.

nature research

Corresponding author(s): Christopher J. Rhodes

Last updated by author(s): Apr 1, 2020

Reporting Summary

Nature Research wishes to improve the reproducibility of the work that we publish. This form provides structure for consistency and transparency in reporting. For further information on Nature Research policies, see Authors & Referees and the Editorial Policy Checklist.

Statistics

For all statistical analyses, confirm that the following items are present in the figure legend, table legend, main text, or Methods section.

n/a	Confirmed	
☐	☒	The exact sample size (*n*) for each experimental group/condition, given as a discrete number and unit of measurement
☐	☒	A statement on whether measurements were taken from distinct samples or whether the same sample was measured repeatedly
☐	☒	The statistical test(s) used AND whether they are one- or two-sided *Only common tests should be described solely by name; describe more complex techniques in the Methods section.*
☒	☐	A description of all covariates tested
☐	☒	A description of any assumptions or corrections, such as tests of normality and adjustment for multiple comparisons
☐	☒	A full description of the statistical parameters including central tendency (e.g. means) or other basic estimates (e.g. regression coefficient) AND variation (e.g. standard deviation) or associated estimates of uncertainty (e.g. confidence intervals)
☐	☒	For null hypothesis testing, the test statistic (e.g. *F*, *t*, *r*) with confidence intervals, effect sizes, degrees of freedom and *P* value noted *Give P values as exact values whenever suitable.*
☒	☐	For Bayesian analysis, information on the choice of priors and Markov chain Monte Carlo settings
☒	☐	For hierarchical and complex designs, identification of the appropriate level for tests and full reporting of outcomes
☒	☐	Estimates of effect sizes (e.g. Cohen's *d*, Pearson's *r*), indicating how they were calculated

Our web collection on statistics for biologists contains articles on many of the points above.

Software and code

Policy information about availability of computer code

Data collection	RNAseq data (BCL files) was collected from a NextSeq instrument using the Illumina NextSeq System Suite (v 2.1). BCL files were demultiplexed and converted to fastq files using the bcl2fastq (v 2.1) conversion software by Illumina. For metabolomics, samples were analyzed using an LC-MS platform consisting of an Ultimate 3000 chromatography system (Thermo, UK) coupled to an AB4000 triple quadrupole mass spectrometer (ABSciex, UK). For phosphoproteomics, samples were analyzed on an EASY nanoLC system coupled with a Fusion Lumos Tribrid orbitrap MS instrument or a Q-Exactive HF MS instrument. For lipidomics, lipids were analyzed on a Sciex SelexIon-5500 QTRAP operated in multiple reaction monitoring mode with both positive and negative mode electrospray.
Data analysis	For RNAseq profiling studies, sequence data was aligned and quantified with RSEM (v 1.2.30) and STAR (v 2.5.2a), respectively. Fastq files were submitted to RSEM/STAR using bash scripts and a PBS job scheduler on a Linux cluster. Data analysis was performed exclusively in R (v 3.4). For differential expression, the limma package was applied in R using the lmFit, decideTests, and eBayes functions. For signature analysis, the GSVA package was applied in R, and differential statistics were derived using the stats functions aov, TukeyHSD or glht (for Dunnet's p-values). Heatmaps were generated in R using the pheatmap function. R code is available upon request. For metabolomics, raw data was analyzed and peak integration performed with the software package MultiQuan (v2.0.2; Applied Biosystems/MDS Sciex). Peak areas were exported into Microsoft Excel for normalisation and further data processing (F-test, t-test, fold-change). For phosphoproteomics, LC-MS/MS raw data files were searched using Proteome Discoverer (PD) (v 2.2). The raw data were searched in PD using a workflow where the raw data were first subjected to database searching using an in-house Mascot server (v 2.2.04, Matrix Science Ltd., London, UK). The in-built ANOVA test in PD was used to generate p-values for all the phosphopeptides analyzed here. With

low number of replicates (e.g. pooled liver samples) the ANOVA test was performed so that the ratio of a protein or peptide is compared to 200 protein/peptide ratios with approximately the same intensity, providing more reliable p-values for low number of replicates.

Additional analysis and creation of plots of primary data was performed in Graphpad Prism (v 7).

For manuscripts utilizing custom algorithms or software that are central to the research but not yet described in published literature, software must be made available to editors/reviewers. We strongly encourage code deposition in a community repository (e.g. GitHub). See the Nature Research guidelines for submitting code & software for further information.

Data

Policy information about availability of data

All manuscripts must include a data availability statement. This statement should provide the following information, where applicable:

- Accession codes, unique identifiers, or web links for publicly available datasets
- A list of figures that have associated raw data
- A description of any restrictions on data availability

The datasets generated during these studies are available from the corresponding author on reasonable request. These datasets include: in vivo data for the mouse studies and encompass metabolic, biochemical and histological data/images; mass spectrometry data from mouse liver and/or serum, mouse hepatocytes or human hepatocytes; imaging and quantitation data for mitochondrial analyses; qRT-PCR data for select gene expression analyses. RNAseq datasets are available in the SRA database with accession number PRJNA574649 and will go public upon publication of this manuscript or 1 year following submission to SRA.

Field-specific reporting

Please select the one below that is the best fit for your research. If you are not sure, read the appropriate sections before making your selection.

☒ Life sciences ☐ Behavioural & social sciences ☐ Ecological, evolutionary & environmental sciences

For a reference copy of the document with all sections, see nature.com/documents/nr-reporting-summary-flat.pdf

Life sciences study design

All studies must disclose on these points even when the disclosure is negative.

Sample size

For in-house in vivo studies presented in Figure 1, 7 and 8 we used sample data comparing NASH vehicle v NASH dulaglutide (GLP-1 monoagonist) in a two group Satterthwaite t-test with a 0.050 one-sided significance level to determine cover 80% of greater power to detect meaningful biological differences for liver lipid percent content and plasma ALT.

For ALT a sample size of 10 in each group will have 80% power to detect a difference in means of 339.000 (the difference between a Group 1 mean, ⊡1, of 1159.000 and a Group 2 mean, ⊡2, of 820.000) assuming that the Group 1 standard deviation, ⊡1, is 190.220 and the Group 2 standard deviation, ⊡2, is 336.090 (ratio of Group 2 to Group 1 standard deviation is 1.767) using a two group Satterthwaite t-test with a 0.050 one-sided significance level.

For liver lipid percent a sample size of 8 in each group will have 80% power to detect a difference in means of 3.000 (the difference between a Group 1 mean, ⊡1, of 33.800 and a Group 2 mean, ⊡2, of 30.800) assuming that the Group 1 standard deviation, ⊡1, is 1.540 and the Group 2 standard deviation, ⊡2, is 2.560 (ratio of Group 2 to Group 1 standard deviation is 1.662) using a two group Satterthwaite t-test with a 0.050 one-sided significance level.

Based on these calculations and the availability of animals at the time we used:
Fig 1: WT Vehicle (n=7); WT Cotadutide (n=8); WT Liraglutide (n=7); WT g1437 (n=7); WT Liraglutide+g1437 (n=7); KO Vehicle (n=8); KO Cotadutide (n=9); KO Liraglutide (n=8); KO g1437 (n=8); KO Liraglutide+g1437 (n=7).

Fig 7 and 8: LFD (n=8); Vehicle (n=11); Cotadutide (n=7); Liraglutide (n= 10); AMLN-to-LFD, Vehicle (n=10).

For the in-house in vivo study presented in Figure 2 sample sizes were determine from the pilot study presented in Supplementary Fig. 2. Based on the hepatic glycogen time-course an n=4 mice per group was determined to be sufficient to achieve statistically significant changes over time.

For figure 3, studies were performed at the Vanderbilt Mouse Metabolic Phenotyping Center. Their rationale is as follows: Based upon extensive experience in the MMPC for the past 10 years, we have determined that to see a 38% difference in a major variable whose standard deviation is 25%, such as muscle glucose uptake, based on the power calculation we will need ~10 successful animals/gender in each group (statistical power = 90%; alpha error = 5%). Our success rate is 70%. This success rate is based upon our extensive experience in the MMPC with the catheterization of mice and assessment of glucose flux. Thus, we will need 10 animals/gender/protocol (total of 80 mice).

For figure 6, the study was performed at Gubra (Hørsholm, Denmark). Sample size was determined using prior data of a biologically relevant difference in NAFLD/NASH score of 1%. With a standard deviation of experimental groups=1, alpha=0.05 and power=0.8 the calculated sample size was n=10. Since the study consisted of pre- and post-treatment liver biopsy and was an IND-enabling study the decision was made to use n=12 to ensure success of the study.

Data exclusions

Figure 3 outliers were selected based on pre-established "Average -/+1.5*SD". This is based on extensive experience of the Vanderbilt MMPC where standard deviation of muscle glucose uptake is ~25%. No data were excluded from other analyses.

Replication	The study presented in Supplementary figure 2 was replicated with additional treatment groups and presented as Figure 2. There were no other attempts to replicate any of the preclinical mouse studies. Cell-based studies were replicated at least three independent times, except for Figure 7d that was replicated twice. The number of replicates are specified in each figure legend. Each replication of in vitro studies yielded similar results.
Randomization	AMLN ob/ob mice were randomized to treatment groups based on body weight, baseline plasma ALT levels and blood glucose levels. AMLN B6 mice were randomized to treatment groups based on baseline biopsy liver fibrosis and steatosis scores, and body weight.
Blinding	Investigators were not typically blinded to treatment arms during the in-life portion of the experiments due to the logistics of the experimental protocol and necessity of the same investigator to prepare the compounds and dose the animals as well as monitor body weight loss for ethical purposes. Pathology evaluation of baseline biopsy and terminal liver tissue was performed in blinded fashion.

Reporting for specific materials, systems and methods

We require information from authors about some types of materials, experimental systems and methods used in many studies. Here, indicate whether each material, system or method listed is relevant to your study. If you are not sure if a list item applies to your research, read the appropriate section before selecting a response.

Materials & experimental systems

n/a	Involved in the study
☐	☒ Antibodies
☐	☒ Eukaryotic cell lines
☒	☐ Palaeontology
☐	☒ Animals and other organisms
☒	☐ Human research participants
☒	☐ Clinical data

Methods

n/a	Involved in the study
☒	☐ ChIP-seq
☒	☐ Flow cytometry
☒	☐ MRI-based neuroimaging

Antibodies

Antibodies used	Anti-CD68 (ab125212, lot# GR77386-35; Abcam, Cambridge, MA; 0.25ug/mL), anti-collagen type 1 (1310-01, lot# J7313-PK; Southern Biotech, Birmingham, AL; 0.4ug/mL) and anti-alpha-SMA (Ab124964, lot# 124973; Abcam, Cambridge, MA; 1:800 dilution).
Validation	All antibodies were sourced commercially. Validation documents can be found as follows anti-CD68: https://www.abcam.com/cd68-antibody-ab125212.html; anti-collagen type 1 A1: https://www.southernbiotech.com/?catno=1310-01&type=Polyclonal#&panel1-5&panel2-1; anti-alphaSMA: https://www.abcam.com/alpha-smooth-muscle-Actin-antibody-EPR5368-BSA-and-Azide-free-ab220795.html

Eukaryotic cell lines

Policy information about cell lines

Cell line source(s)	Freshly isolated primary human hepatocytes from healthy and NASH donors were procured from Samsara Sciences (San Diego, CA). Mouse primary hepatocytes were freshly isolated at MedImmune (Gaithersburg, MD).
Authentication	Documentation as to donor history and pathology report was supplied by Samsara Sciences (San Diego, CA)
Mycoplasma contamination	Human cell donors were either listed as not reported or not positive for bacterial presence (Samsara Sciences). Freshly isolated mouse hepatocytes were not tested.
Commonly misidentified lines (See ICLAC register)	All in vitro studies were performed in isolated primary hepatocytes and are not listed in the ICLAC database.

Animals and other organisms

Policy information about studies involving animals; ARRIVE guidelines recommended for reporting animal research

Laboratory animals	All animals in these studies were male C57BL6J mice. Strains were either diet-induced obese mice, aged ~20 weeks, NASH-induced mice aged ~35 weeks at end of study, or leptin-deficient ob/ob mice aged ~24 weeks.
Wild animals	None
Field-collected samples	None
Ethics oversight	Animal studies were approved by either the Institutional Animal Care and Use Committee at MedImmune/AstraZeneca (Gaithersburg, MD) or Vanderbilt University (Nashville, TN) in accordance with Animal Welfare Act guidelines, or Gubra

(Hørsholm, Denmark) under personal licenses issued by the Danish Committee for Animal Research.

Note that full information on the approval of the study protocol must also be provided in the manuscript.